ARTICLE OPEN

Check for updates

Exfoliation of an extruded Mg-4Li-1Ca alloy in presence of glucose and bovine serum albumin

Lei Cai[1], Mei-Qi Zeng[1], Meng-Jie Liu[1], Jing-Yu Bao[1], Yu-Qian Ren[1], M. Bobby Kannan[2], Lan-Yue Cui[1], Cheng-Bao Liu[1], Fen Zhang[1], Shuo-Qi Li[1] and Rong-Chang Zeng[1]✉

Exfoliation corrosion (EFC) on extruded Mg-4Li-1Ca alloys as bone implant materials has not been reported. This study aimed to elucidate the degradation mechanism of a corrosion type-exfoliation occurred on an extruded Mg-4Li-1Ca alloy under the interaction of glucose (Glu) and bovine serum albumin (BSA) in Hank's solution. The alloy microstructure, chemical composition, texture, stress distribution and Volta potential maps were characterized using metallographic microscopy, scanning electron microscopy and electron backscattered diffraction, and scanning Kelvin Probe. The alloy corrosion behavior was investigated via electrochemical testing and hydrogen evolution rate methods. X-ray diffraction, Fourier transform infrared spectrometry, X-ray photoelectron spectrometer, and fluorescence microscopy were used to analyze the corrosion products and the adsorption of the organic molecules. The experimental results indicated that the anodic second phase (Mg_2Ca) were distributed in lamellar and rod-like patterns along the extrusion direction of the alloy, a lower Volta potential for Mg_2Ca, texture and residual stresses also promote EFC. An increase in Glu concentration exacerbated the EFC, whereas BSA inhibited the EFC of the alloy. Higher Glu concentrations in BSA in turn inhibited EFC since Glu can complex with amino acids in proteins to form Glu-amino acid amides, which promoted protein adsorption and thereby forming a dense protective film on the alloy surface. The preferential dissolution of the Mg_2Ca phase particles led to the complexation and adsorption of Glu and protein. This study enriches the understanding of the corrosion types in biomedical Mg-4Li-1Ca alloy and paving the way for enhancing the EFC resistance of the alloy.

npj Materials Degradation (2024)8:8 ; https://doi.org/10.1038/s41529-024-00425-1

INTRODUCTION

Magnesium (Mg) alloys are widely utilized in the aerospace, automotive, and electronics industries due to their high specific strength, stiffness, and damping capacity[1–3]. Additionally, their excellent biocompatibility and favorable mechanical properties make them promising candidates for biomedical applications[4–8]. However, the electrode potential of Mg is only −2.37 V vs. SHE, which renders them susceptible to corrosion and therefore, limits their practical applications[9].

Generally, Mg alloys are susceptible to various types of corrosion, including galvanic corrosion[10], pitting corrosion[11,12], intergranular corrosion (IGC)[13], exfoliation corrosion (EFC)[14,15], dealloying corrosion (DAC)[16], stress corrosion cracking[17], filiform corrosion[18,19], corrosion fatigue[20], and crevice corrosion[21]. However, IGC, EFC, and DAC have been scarcely reported on the corrosion of Mg alloys[18,22].

IGC is a form of localized corrosion caused by micro-galvanic corrosion and is closely related to the size and distribution of the intermetallic particles. EFC is a special form of IGC that occurs on elongated grains and extruded alloys. This form of corrosion has been extensively studied in aluminum alloys[23]. It was believed that Mg alloys do not exhibit EFC[24]. Recently, our group[14] reported that EFC occur in Mg-1Li-1Ca after a long exposure to 3.5 wt. % NaCl solution. Song et al.[25] noted that the observation of EFC in extruded Mg-Li-Ca alloys is a significant advance in the field of Mg alloy corrosion. However, this study lacked in-depth analysis of microstructural aspects, including characterization of the texture and the influence of stress. In addition, EFC can lead to a drastic decrease in mechanical properties, making it impossible to ensure the complete support of the material during its service life. Herein, it is of necessity to study the possibility of EFC before using a particular alloy.

The addition of Lithium (Li) in Mg alloys is beneficial not only to reduce their mass but also enhance their strength via solid-solution strengthening[26]. The first in vivo study performed by Witte et al.[27] demonstrated that the Mg-Li-RE (LAE442) alloy is more corrosion-resistant than the AZ91 alloy. However, RE is usually toxic. The replacement of calcium (Ca) may be a good choice for RE in Mg-Li alloys.

Ca in Mg alloys has grain-refining effect and improve the alloy strength and formability, and also enhance the biocompatibility of the alloy since Ca is non-toxic and it is the primary component of human bones[9,28].

In our previous investigation[29] shows that Mg-Li-Ca alloys have corrosion resistance superior to Mg-Ca alloys in Hank's solutions. Our another study firstly reveals the formation of Li_2CO_3 on Mg-Li-Ca alloys and the transformation of pitting corrosion to general corrosion due to the grain refinement[30]. Long et al.[31] investigated that Mg-4Li-1Ca has a larger UTS, a larger EL and a lower corrosion rate than Mg-1Li-1Ca in Hank's solution. This scenario strongly supports the hypothesis that Li plays a positive role in decreasing the degradation rate and changing the corrosion type of biomedical Mg-Li-Ca alloys.

Furthermore, the consequence of biocompatibility of Mg-(1, 9, 15)Li-Ca alloys exhibits no toxicity to L-929 cells in 10% concentration of extracts, an acceptable hemolysis ratio for the Mg-1Li-1Ca alloy, and no sign of thrombogenicity for the Mg-(1, 9) Li-Ca alloys except for the Mg-15Li-1Ca alloy[32]. Namely, low content of Li in Mg alloys might be more biocompatible.

[1]Corrosion Laboratory for Light Metals, School of Materials Science and Engineering, Shandong University of Science and Technology, Qingdao 266590, China. [2]School of Engineering, University of Newcastle, Callaghan, NSW 2308, Australia. ✉email: rczeng@foxmail.com

Further in vivo study[33] disclosed that Mg-3.5Li-0.5Ca alloys possess the best in vitro performance for the implants into the mice femurs after 0.5 and 2 months, and a markable growth in cortical bone thickness on the implanted Mg-3.5Li-0.5Ca alloy rods. The extracts of the Mg-3.5Li-0.5Ca alloy are helpful for the osteogenic differentiation of human bone marrow-derived mesenchymal stem cells along the canonical Wnt/β-catenin pathway. Hence, Mg-4Li-Ca alloy has the greatest potential for use in bone implantation applications[34].

Nowadays, China is the world's largest country in terms of diabetes prevalence, with 141 million reported cases of diabetes in 2021 and an adult prevalence rate of 12.8%, accounting for 26.2% of the total number of reported cases worldwide, which is expected to continue to grow to 164 million and 174 million in 2030 and 2045[35]. The ageing population and the large number of people suffering from hyperglycemia and diabetes make it a major public health problem with considerable implications for the country's economic development, social security and stability[36,37]. Elevated blood glucose (Glu) levels in humans inhibit bone calcium absorption and mineralization, leading to osteoporosis and an increased risk of fractures, particularly in hyperglycemic and diabetic patients and the elderly[38]. Therefore, investigating the in vitro corrosion behavior of biomedical Mg alloys in Glu-containing environments has important implications for their practical application. Our previous studies[39–44] have demonstrated the significant impact of Glu, amino acids and proteins on the corrosion behavior of Mg alloy bone implants. Glu, as a polyhydroxy aldehyde and monosaccharide is an energy source and intermediate product of metabolism in living cells. The presence of Glu influences the corrosion degradation behavior of pure Mg and its alloys in simulated body fluids[39]. Specifically, Glu reduces the pH of the solution, which increases the corrosion rate of pure Mg and its alloys in physiological saline but decreases the corrosion rate in Hank's solution[39]. This is due to the acidification of the Mg surface by Glu, which converts its aldehyde group into a carboxyl group that facilitates interfacial reactions of Mg alloys. This promotes the formation of Ca-P salts and hydroxyapatite (HA)[45].

Proteins are organic macromolecules that are essential for human metabolism. Many studies have investigated the influence of proteins on the degradation rate of Mg alloys in different environments. It is widely reported that the degradation behavior of Mg alloys is primarily affected by protein adsorption and chelation[46–49]. Proteins act as a diffusion barrier between the metal surface and the surrounding environment by adsorbing onto the surface of the Mg alloy[47,48]. This process inhibits the adsorption of corrosive ions, and ultimately reducing the corrosion rate of Mg alloys. The reaction between the Mg alloys and proteins is dependent on various factors such as the type of Mg alloy, reaction time, and environmental conditions[4]. Protein adsorption occurs in the initial stages of interaction with the Mg alloy surface, and the adsorbed proteins can alter the physical morphology and chemical properties of the Mg alloy surface, and thereby affecting its degradation behavior. In fact, the interaction between proteins and the Mg alloys is a more complex process.

Some studies have suggested that proteins can chelate Mg^{2+} ions, and accelerate the degradation rate of Mg alloys. In contrast, another research has shown that proteins can react with Mg^{2+} ions $(RCH(NH_2)COO)_2Mg$, and inhibit the degradation behavior of Mg alloys[50]. Furthermore, protein adsorption can affect subsequent cell adhesion, proliferation, differentiation, signaling, and tissue regeneration on the surface of Mg alloys. Sivaraman et al.[51] demonstrated that the conformation of adsorbed proteins is the primary determinant of platelet adhesion rather than the amount adsorbed. Similarly, Hu et al.[52] reported that different bioactive surfaces induce conformational changes in adsorbed proteins, and different conformations have a significant effect on cellular activity. Despite the potential impact of Glu and proteins on the conformational changes of Mg alloys, only a few studies have investigated this phenomenon in pure Mg. Our group[41] examined the coupling effect of amino acids and Glu on the degradation behavior of pure Mg in physiological saline, and also[43] investigated the impact of Glu and protein on the degradation of pure Mg and found that the presence of Glu and protein together significantly inhibited the degradation of Mg, resulting in a reduced degradation rate. Further understanding of the mechanisms involved in protein adsorption and chelation can provide insights for the design and development of Mg alloys with improved corrosion resistance for various biomedical applications.

This work aims to investigate the effect of Glu and protein on the EFC behavior of Mg-4Li-1Ca in physiological environment. The influence of factors such as alloy texture, stress, and second phase on EFC is also analyzed in-depth from the microstructure. Based on the detailed analysis of the experimental results, a mechanism for EFC on the alloy involving Glu and protein coupling has been proposed.

RESULTS

Figure 1a–c depicts the metallographic micrographs of the Mg-4Li-1Ca alloy, showing the top surface, longitudinal, and transverse sections (Supplementary Fig. 1). The intermetallic compounds or second phases (Mg_2Ca particles) were observed mainly at the grain boundaries along the extrusion direction (Fig. 1a). In the LS sample, the Mg_2Ca particles were distributed in lines parallel to the extrusion direction; and in the TS sample, the Mg_2Ca particles were distributed in flat, short bars perpendicular to the extrusion direction. The lamellar pattern of Mg_2Ca particles distribution in the Mg-4Li-1Ca alloy provides a structural factor for EFC as the Mg_2Ca particles act as the anodic phase relative to the α-Mg matrix and is preferentially corroded during the corrosion process[14,31,53]. From the electron probe X-ray microanalysis (EPMA) (Fig. 1e–g), it was observed that the intermetallic particles Mg_2Ca were linearly distributed in the Mg-4Li-1Ca alloy along the extrusion direction, and the enrichment of Ca element at the location of the second phase was seen from the line scan X-ray spectroscopy (EDS), which indicated that the presence of the Mg_2Ca phase, and the peak of Mg_2Ca was visible in the X-ray diffraction (XRD) plot (Fig. 1d).

Scanning Kelvin probe (SKP) testing was employed to detect the Volta potential in a specific region of the sample and characterize the corrosion reaction activity. Supplementary Fig. 2 illustrates the Volta potential plots for the extruded Mg-4Li-1Ca alloy in SS, LS, and TS samples. The low potential dots and short bars in the Mg-4Li-1Ca TD-ED plane correspond to the intermetallic Mg_2Ca in Fig. 1a, which exhibit the lowest Volta potential. This suggests that the corrosion pits may start first in the planar Mg_2Ca particles during the corrosion process of the extruded Mg-4Li-1Ca alloy.

In the LS and TS of the extruded Mg-4Li-1Ca alloy (Supplementary Fig. 2), a gradual increase in potential from the outer to the inner layer was evident. The lowest Volta in the LS is −488 mV, and in the TS, it was −1027 mV. The highest and lowest Volta potentials in the LS had a difference of 390 mV, and in the TS, the Volta potential difference was 710 mV. It was thus evident that the outer region had lower reaction activity than the inner region.

The microstructural characteristics of the Mg-4Li-1Ca alloy were investigated using grain orientation analysis, and the results are presented in Fig. 2. The SS plane of the alloy (Fig. 1a) showed a relatively uniform distribution of grain orientation, dominated by the {0001} base plane. This plane is known for its strong corrosion resistance as compared to the prismatic and conical planes[54–56]. In contrast, the LS and TS planes (Fig. 1b, c) exhibited a dominant grain orientation of $\{\bar{1}2\bar{1}0\}$ and $\{01\bar{1}0\}$, respectively. The LS plane showed a clear grain-cutting along the extrusion direction, while the TS plane showed some grain orientation along the same

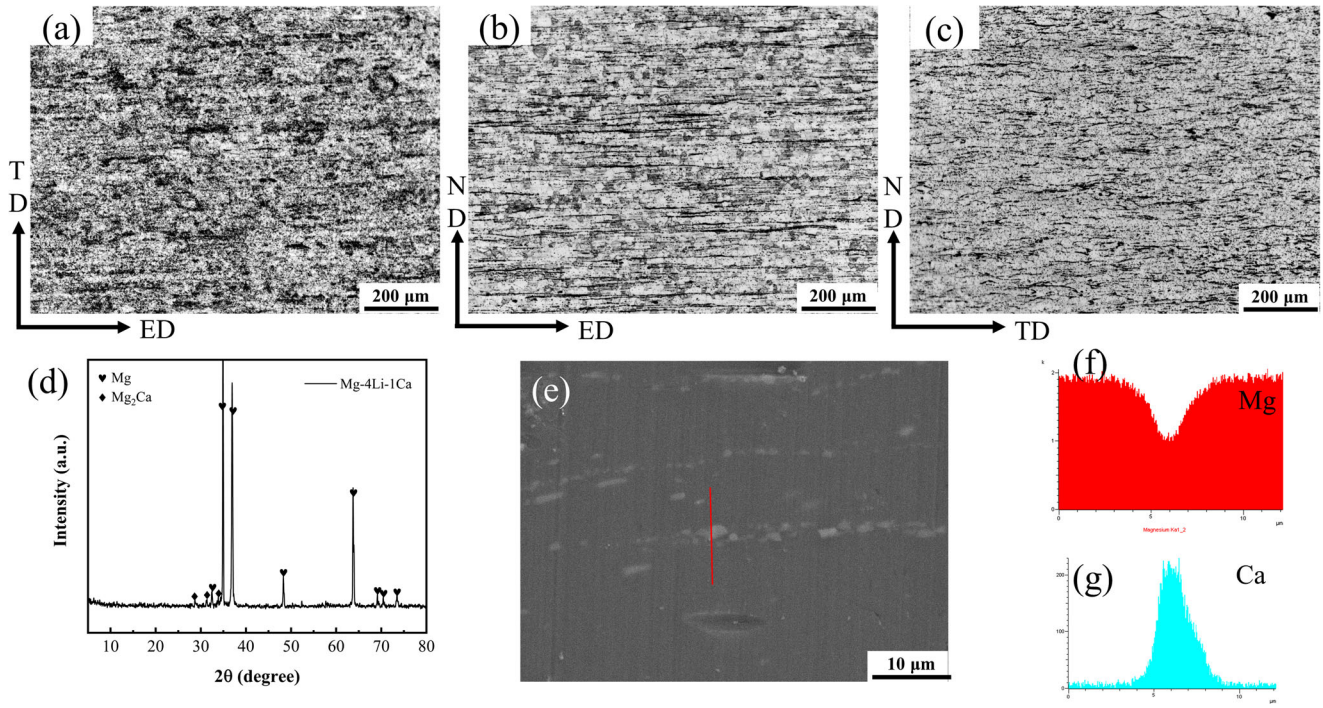

Fig. 1 Microstructure of Mg-4Li-1Ca alloy. OM diagram: **a** surface section (TD-ED), **b** longitudinal section (ED-ND) and **c** transverse section (TD-ND); **d** XRD, **e** cross-sectional EPMA image and **f**, **g** line-scan EDS, indicating the linear distribution of the intermetallic particles Mg_2Ca along the extrusion direction.

direction. The average grain size was found to be ~5.84 μm for SS, 9.71 μm for LS, and 8.09 μm for TS, with LS and TS having larger grain sizes than the average size of SS (Supplementary Fig. 3). Furthermore, the grain orientation, polar, and antipodal diagrams indicated that the extruded Mg-4Li-1Ca alloy had a distinct texture.

From Supplementary Fig. 4, it can be observed that the local misorientation on the surface is greater than that on the longitudinal and transverse sections. The local average misorientation (LAM) analysis also revealed that the surface had the highest local dislocation density. As the local dislocation density was directly proportional to residual stress, it can be concluded that the surface has the highest residual stress, with all three faces exhibiting residual stress. And the above equation gives ρ^{GND} of 4.0, 2.24, and $1.68 \times 10^{14}\,m^{-2}$ for SS, TS, and LS surfaces, respectively (Supplementary Fig. 4)[57–60]. Furthermore, the longitudinal and transverse sections showed orientation-dependent distribution of residual stress along the extrusion direction, which might provide high-energy corrosion sites for subsequent corrosion studies.

Figure 3 illustrates the HER curves of the Mg-4Li-1Ca alloy in Hank's solution with different concentrations of Glu content and containing BSA at 37 °C. The HER curve can be used to characterize the change in the degradation rate of the alloy. The samples displayed higher degradation rate values at the beginning of the immersion test, which may be due to the preferential corrosion of the anodic second phase in the Mg-4Li-1Ca alloy, releasing H_2. The degradation rates of the samples were: 3 g·L^{-1} Glu > 2 g·L^{-1} Glu > 1 g·L^{-1} Glu > 1 g·L^{-1} Glu + BSA > 2 g·L^{-1} Glu + BSA > 3 g·L^{-1} Glu + BSA solution. It was observed that the corrosion rate of the Mg-4Li-1Ca alloy increased with increasing Glu concentration in the Hank's solution, while the addition of BSA slowed down the corrosion of the alloy and the corrosion rate decreased with increasing Glu concentration. This was associated with the properties of Glu in solution, where it underwent acidification and was converted to gluconic acid. The adsorption of gluconic acid on the surface of the Mg alloy promoted the adsorption of Cl^- ions, which accelerated the corrosion[39]. In contrast, with the addition of BSA, adsorption of BSA occurred on the surface of the Mg alloy and the synergistic effect of BSA with Glu[43] resulted in slowing down the onset of corrosion.

Open circuit potential (OCP), potentiodynamic polarization tests (PDP), and Electrochemical Impedance Spectroscopy (EIS) were employed to investigate the degradation behavior of Mg-4Li-1Ca alloy in six distinct solutions (Fig. 4 and Supplementary Tables 2, 4). The OCP curves of Mg-4Li-1Ca in all the six solutions exhibited a continuous rise and then stabilized with only small variations which indicates that Mg dissolves and gradually forms a corrosion product layer at the interface until it reaches a steady state[61]. The OCP values were found to be the highest in 1 g·L^{-1} Glu, followed by 2 g·L^{-1} Glu and 3 g·L^{-1} Glu, with the degradation of Mg-4Li-1Ca being most prominent in the early stages of degradation.

The PDP results indicated that Mg-4Li-1Ca alloy exhibited the highest E_{corr} and lowest i_{corr} in 1 g·L^{-1} Glu, whereas in 3 g·L^{-1} Glu, the alloy showed the lowest E_{corr} and highest i_{corr}, implying that Mg-4Li-1Ca alloy degraded the slowest in 1 g·L^{-1} Glu solution and the fastest in 3 g·L^{-1} Glu solution. In contrast, in solutions containing BSA, the degradation rate was found to be slowest in 3 g·L^{-1} Glu + BSA due to its highest E_{corr} and lowest i_{corr}, while the opposite was true in 1 g·L^{-1} Glu + BSA. As the Glu content decreased, the anodic branch moved towards the noble region, whereas in the solution containing BSA, the anodic branch moved towards the noble region as the Glu concentration increased. This suggests that the corrosion of the alloy is spontaneous when Glu concentration increased or when Glu concentration decreased in solutions containing BSA.

EIS tests were carried out on three faces of the Mg-4Li-1Ca alloy (SS, LS, TS) and the results are shown in Supplementary Fig. 5. The circuit fit was carried out and the fitted circuit is shown in the inset of Supplementary Fig. 5a and Supplementary Table 3. LS had the highest radius of capacitive arc resistance, the largest |Z|, and as can be seen in the circuit fitting data, LS had the greatest charge transfer resistance (R_{ct}), indicating that LS surface had the best corrosion resistance. The results of the Nyquist, Bode and Bode

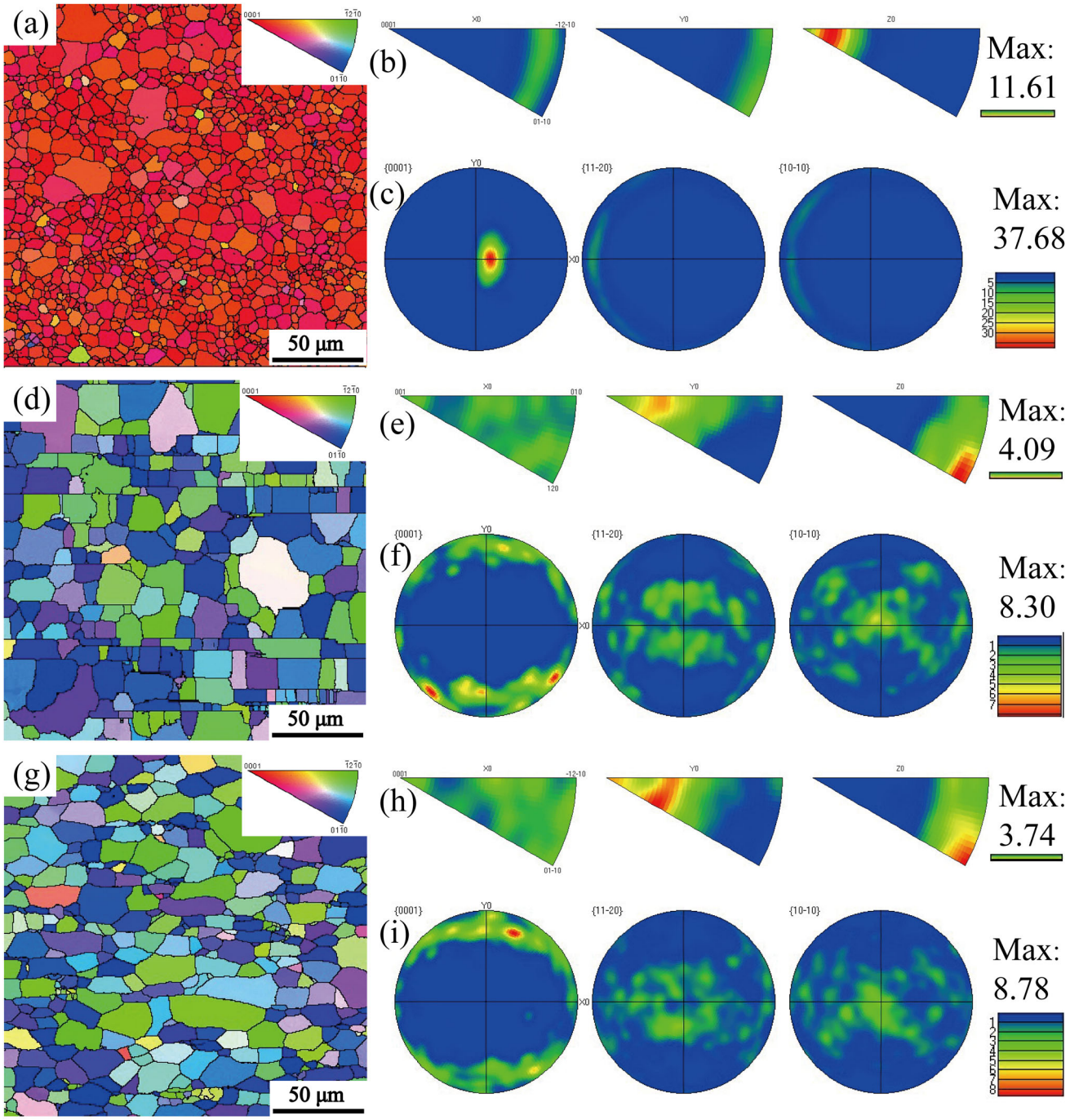

Fig. 2 EBSD information for different surfaces of Mg-4Li-1Ca alloy. Grain orientation: **a** SS, **d** LS and **g** TS, polarity: **b** SS, **e** LS and **h** TS and antipolarity maps: **c** SS, **f** LS and **i** TS for Mg-4Li-1Ca alloys with different surfaces.

phase plots are consistent, with the LS face having the best corrosion resistance and the TS face having the worst corrosion resistance.

Figure 4e, f present the EIS curves for Mg-4Li-1Ca alloy in different solutions. The Nyquist plots for the Mg-4Li-1Ca alloy in each of the six solutions contain high-frequency reactance, low-frequency reactance and low-frequency susceptibility reactance. The alloy in Hank's solutions with different concentrations of Glu exhibited the largest capacitive arc radius in the 1 g·L^{-1} Glu solution and the smallest in the 3 g·L^{-1} Glu solution, while the solutions containing BSA had the largest and smallest capacitive arc radii in the 3 g·L^{-1} Glu + BSA and 1 g·L^{-1} Glu + BSA solutions, respectively. This indicated that the elevated Glu content accelerated the corrosion of the Mg-4Li-1Ca alloy, while the elevated Glu content in the solution containing BSA inhibited the corrosion of the Mg-4Li-1Ca alloy.

To gain further insight into the corrosion mechanism of the Mg-4Li-1Ca alloy, a circuit fit was carried out and the fitted circuit is shown in the inset of Fig. 4e, f and Supplementary Table 4. L and R_L denote the inductance and resistance, respectively, and are used to describe low-frequency inductive loops[62]. The presence of inductive loops indicates the occurrence of corrosion pits, which is mainly associated with the preferential corrosion of the anodic second phase (Mg_2Ca) of the Mg-4Li-1Ca alloy. The R_{ct} represents

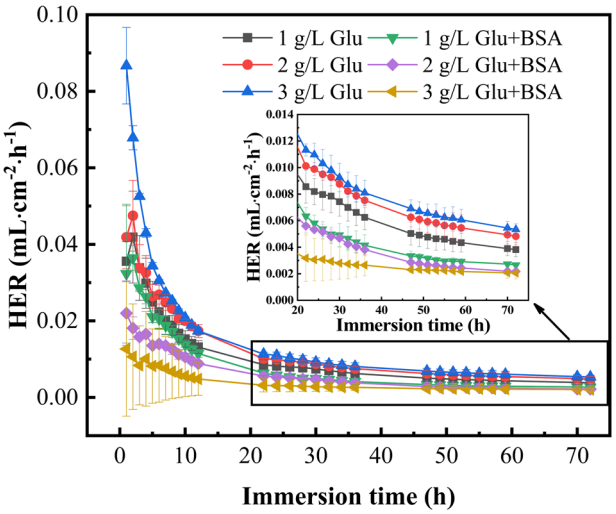

Fig. 3 HER curves. HER curves of Mg-4Li-1Ca alloys immersed in different solutions for 72 h.

the resistance to the transfer of charges and a higher R_{ct} value implies a lower dissolution rate of Mg[63]. The R_{ct} values followed the order: 3 g•L^{-1} Glu < 2 g•L^{-1} Glu < 1 g•L^{-1} Glu, 1 g•L^{-1} Glu+BSA < 2 g•L^{-1} Glu + BSA < 3 g•L^{-1} Glu + BSA. Furthermore, the low-frequency impedance modulus $|Z|$ in the Bode diagram is a key indicator for assessing corrosion resistance, with a higher $|Z|$ indicating better corrosion resistance[64]. It was observed that Z increased in the decreasing order: 3 g•L^{-1} Glu < 2 g•L^{-1} Glu < 1 g•L^{-1} Glu, 1 g•L^{-1} Glu + BSA < 2 g•L^{-1} Glu + BSA < 3 g•L^{-1} Glu + BSA.

Figures 5 and 6 depict the EFC behavior of the Mg-4Li-1Ca alloy in Hank's solutions with varying Glu concentrations or containing BSA after different immersion periods (30, 60, 90, 120, 150, 180 days) at 37 °C. EFC became more severe as the Glu concentration and immersion time increased. The surface layer with finer grains exhibited greater corrosion resistance as compared to the inter layer with coarser granules. This phenomenon may explain why EFC occurred more easily on longitudinal sections with anisotropic microstructures. In other words, the initial corrosion potential differed significantly between the outer surface and the interior, leading to macroscopic galvanic corrosion at the interface between the outer surface and the interior and slight corrosion of the interior. In addition, the preferential dissolution of Mg_2Ca particles along the grain boundaries of the elongated microstructure might be the initiation of corrosion pits. This finding was consistent with our previous report[14], the extruded Mg-1Li-1Ca exhibited EFC in the form of uncorroded Mg alloy flakes buckling from the substrate after 90 D immersion in a 3.5 wt.% NaCl solution, but the EFC was less severe than in the SBF.

The inclusion of BSA resulted in a more uniform corrosion morphology as compared to the localized corrosion observed in the absence of BSA. This can be attributed to the preferential adsorption of BSA on the material, creating a protective layer that prevents the aggressive ions (e.g., Cl^-) from attacking the material. EFC was observed after 120 days in the BSA-containing solution, whereas it occurred in just 30 days in the Hank's solution without BSA. Furthermore, the extent of EFC decreased as the Glu concentration increased, primarily due to Glu promoting the adsorption of BSA on the Mg alloy surface and inhibiting EFC development[43].

Figures 7, 8, Supplementary Figs. 6, 7 present the Scanning electron microscopy (SEM) images and EDS data of the Mg-4Li-1Ca alloy after immersion in various solutions. It was observed that the corrosion product films generated by the Mg-4Li-1Ca alloy after immersion in all the solutions experienced severe rupture. Based on the corrosion morphology of the surfaces immersed in different concentrations of Glu solution for 30 days, it was observed that the higher the Glu concentration, the more corrosion products on the surface, indicating that the increase in Glu concentration promoted the degradation of the Mg-4Li-1Ca alloy. The EDS data revealed that the main elements of the corrosion products in the BSA-free solution were C, O, Mg, P, and Ca, while in the BSA-containing solution, the presence of N was also observed, primarily due to the BSA adsorbed on the surface of the Mg alloy.

Figures 9 and 10 display the cross-SEM images and EDS patterns of the Mg-4Li-1Ca alloy. The cross-SEM images reveal that the Mg-4Li-1Ca alloy experienced significant delamination of Mg when immersed in Hank's solutions with different Glu concentrations for 30, 60, 90, and 120 days. This was primarily due to the preferential corrosion of the lamellar anodic second phase Mg_2Ca-particles distribution in the Mg-4Li-1Ca alloy, resulting in EFC. However, in the BSA-containing solution, the phenomenon of Mg delamination due to EFC was not observed until 120 days, and no significant Mg delamination due to EFC was observed in the 3 g•L^{-1} Glu + BSA solution even after 180 days. This was mainly due to the presence of Glu, which promoted protein adsorption[43] and inhibited the development of EFC.

Fourier transform infrared spectrometry (FT-IR) spectroscopy was utilized to investigate the chemical composition and functional groups of corrosion products on the surface of a sample immersed in different solutions. The FT-IR spectra in Fig. 11 confirm the presence of an $Mg(OH)_2$ film through the Mg-OH stretching vibrations and O-H group absorption bands. The typical vibration modes of Glu molecules were observed through the C-H bands. The $H_2PO_4^-$ and PO_4^{3-} absorption peaks indicated the presence of phosphate in the corrosion products, and the CO_3^{2-} groups in the FT-IR confirmed the presence of carbonates. Additionally, the presence of C=O or C=O/C=N bonds suggested the adsorption of Glu or Glu and BSA onto the surface of the Mg alloy.

Figure 12 displays the XRD patterns of Mg-4Li-1Ca after various immersion times in different solutions. The dominating peaks in all spectra were related to the Mg phase[65]. A small amount of $Mg(OH)_2$ was generated on the surface of Mg-4Li-1Ca in Hank's solution after immersion, as shown by the peaks at 18° and 38°. Furthermore, $MgCO_3$ was present on the surface after different immersion times, mostly due to the formation of $MgCO_3$ by CO_2 and $Mg(OH)_2$. The phosphate and Ca^{2+} in solution generated $Ca(H_2PO_4)_2{\cdot}H_2O$ on the Mg-4Li-1Ca alloy surface.

In Fig. 13, the total X-ray photoelectron spectrometer (XPS) spectrum of the Mg-4Li-1Ca alloy surface after 2 h (h) of immersion, the N1s spectrum in the BSA-containing solution, and the C1s fine spectra of the surface of Mg-4Li-1Ca alloy immersed in different solutions for different times (0.5 h, 2 h, 24 h) are presented. The total spectrum (Fig. 13a) suggests the presence of C, O, Mg, Ca, and P in Hank's solutions with different concentrations of Glu without BSA, while the presence of N was detected in the solution containing BSA, indicating protein adsorption, which was consistent with the EDS results. In the N1s spectrum (Fig. 13b–d), the binding energy of N1s photoelectrons showed three peaks at 399.1 eV, 399.9 eV, and 400.7 eV, corresponding to C=N[66], O=C-NH, and N-O/C-N, respectively. This indicates the adsorption of protein on the Mg-4Li-1Ca alloy surface.

From the C1s fine spectra of the sample surface after immersion in the solution without BSA (Fig. 13e–j), three peaks at 284.8 eV, 285.5 eV, and 288.8 eV, corresponding to C-C/C-H, C-O, and C=O, respectively, can be seen, indicating that Glu underwent acidification and was converted to gluconic acid[39]. In the fine spectrum of C1s containing BSA (Fig. 13h–j), 284.8 eV, 286.3 eV,

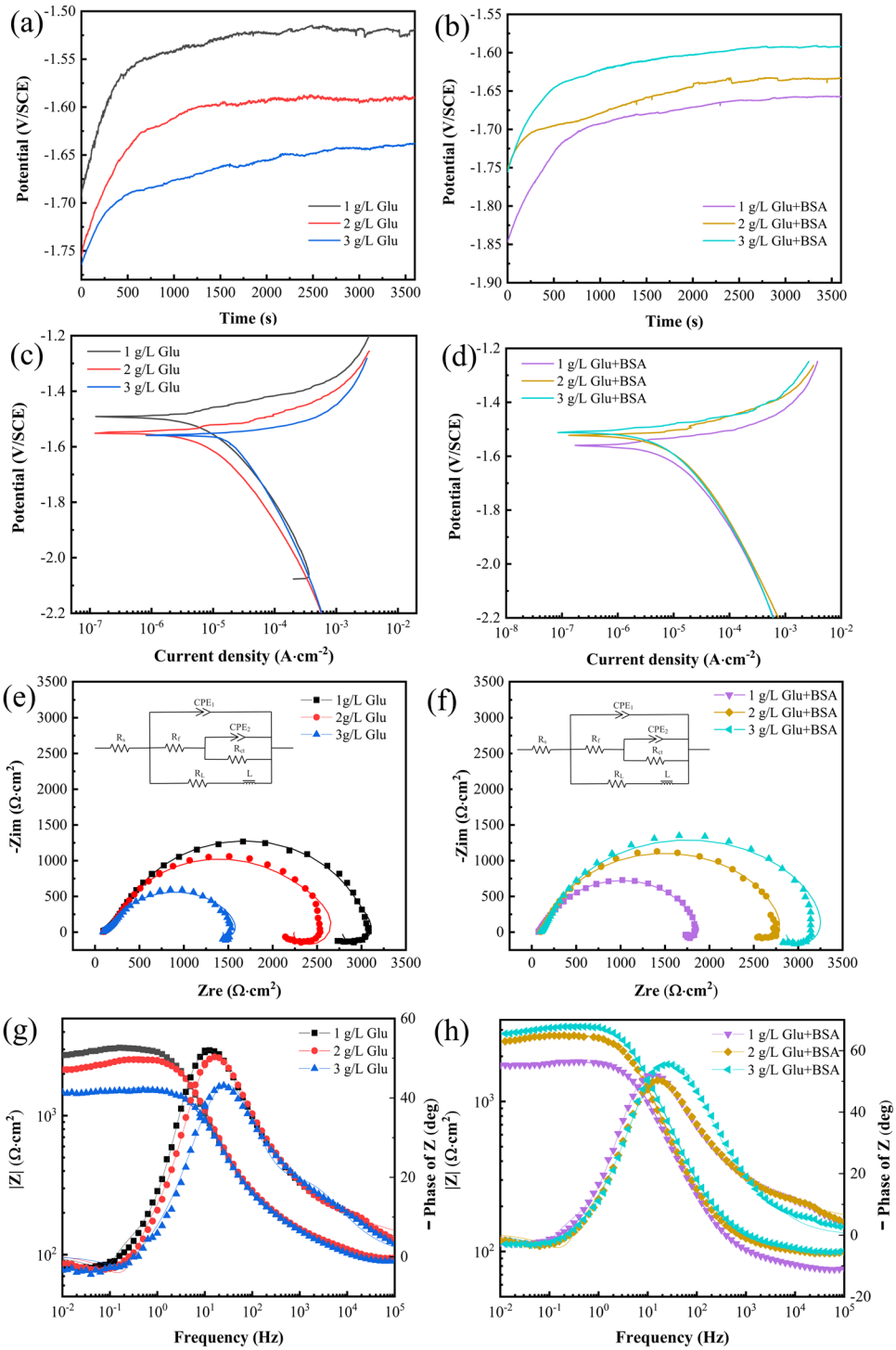

Fig. 4 Electrochemical profiles of Mg-4Li-1Ca alloy immersed in different solutions. Curve of OCP vs. immersion time in **a** Hank's, **b** Hank's + BSA; polarization in **c** Hank's, **d** Hank's + BSA; EIS after immersion in **e**, **f** Hank's, **g**, **h** Hank's + BSA.

288.2 eV and 289.6 eV correspond to the presence of C-C/C-H, C-O, C=O and N-C=O bonds, respectively. This finding suggested the presence of Glu compounds and protein compounds on the surface[43].

The laser confocal microscopy fluorescent image of BSA and Glu adsorption on the Mg alloy surface at various immersion durations is shown in Fig. 14. Fluorescein isothiocyanate for fluorescent labeling of organic molecules[67,68]. As can be seen from Fig. 14, when the Mg-4Li-1Ca alloy was immersed in a solution containing Glu and BSA for 0.5 h, small amounts of Glu and BSA were locally adsorbed on the surface of the sample, and the amount of Glu and BSA adsorbed on the surface of Mg-4Li-1Ca increased with the increase in soaking time. From the adsorption results on the surface as well as the metallographic images and SKP results, Glu and BSA were preferentially adsorbed on the second phase Mg_2Ca particles. And the adsorption points of Glu and BSA were brighter, which indicated that the pre-existing Glu and BSA were more easily adsorbed on the second phase particles. This was mainly

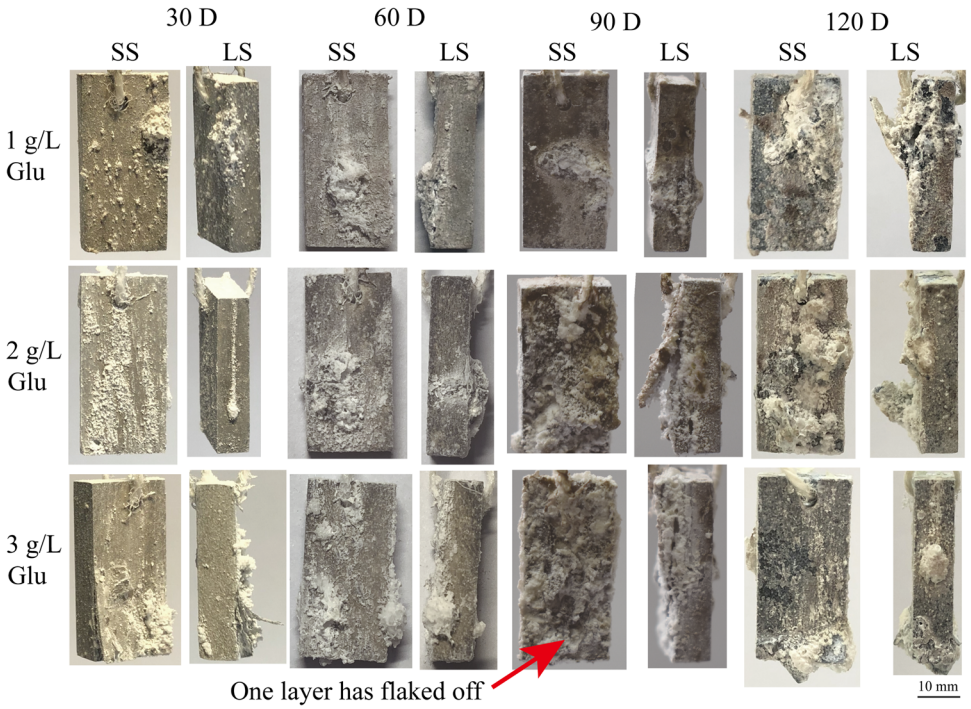

Fig. 5 Macroscopic corrosion morphology pictures. Macroscopic corrosion morphology pictures of the surface of Mg-4Li-1Ca alloy after different immersion times at different concentrations of Glu.

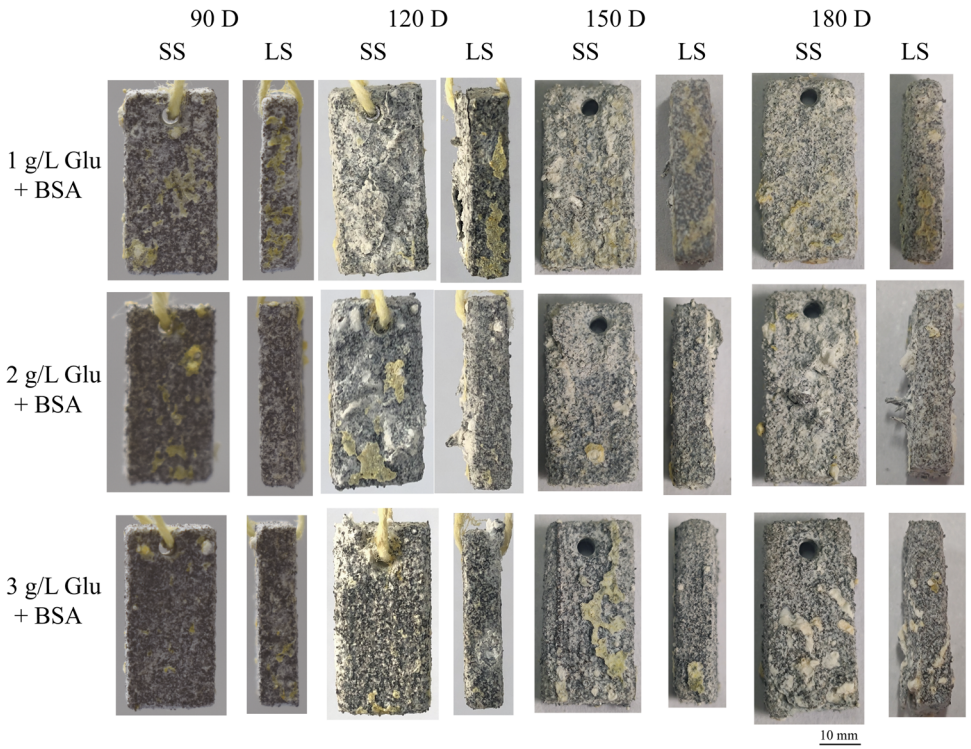

Fig. 6 Macroscopic corrosion morphology pictures. Macroscopic corrosion morphology pictures of the surface of Mg-4Li-1Ca alloy after different immersion times containing BSA at different concentrations of Glu.

because the second phase Mg_2Ca particles was anodic, which preferentially corroded. The fluorescent features appeared in a striped distribution along the extrusion direction after corrosion, which was consistent with the second distribution in the OM images (Fig. 1a–c). The Mg^{2+} and Ca^{2+} generated after corrosion form complexes and adsorb with carboxyl groups in gluconic acid and carboxyl and amino groups in proteins, making Glu and proteins preferentially adsorb at the location of the second phase particles. Accordingly, the increase in Glu content accelerated the adsorption of Glu, while the addition of BSA inhibited the adsorption of both Glu and BSA with the increase in Glu content.

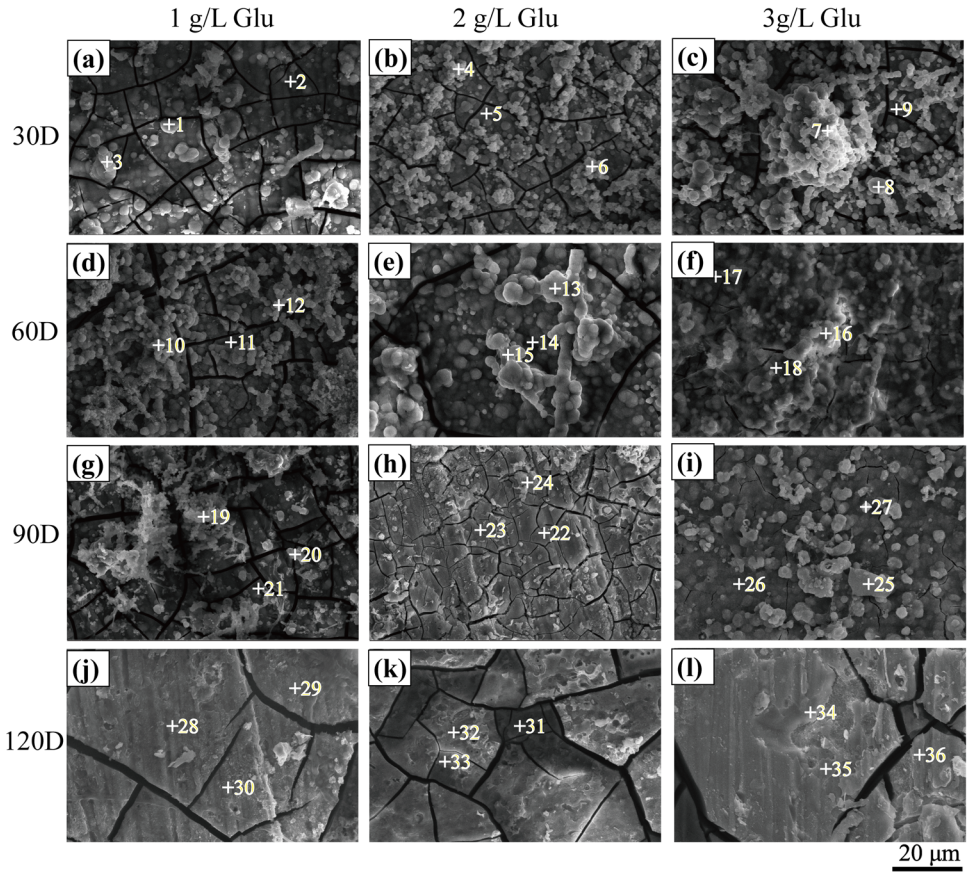

Fig. 7 SEM of the surface of Mg-4Li-1Ca alloy after different immersion times at different concentrations of Glu. a 1 g·L^{-1} Glu 30 D, **b** 1 g·L^{-1} Glu 60 D, **c** 1 g·L^{-1} Glu 90 D, **d** 1 g·L^{-1} Glu 120 D, **e** 2 g·L^{-1} Glu 30 D, **f** 2 g·L^{-1} Glu 60 D, **g** 2 g·L^{-1} Glu 90 D, **h** 2 g·L^{-1} Glu 120 D, **i** 3 g·L^{-1} Glu 30 D, **j** 3 g·L^{-1} Glu 60 D, **k** 3 g·L^{-1} Glu 90 D, **l** 3 g·L^{-1} Glu 120 D.

DISCUSSION

The previous study found that 1, 2, 3 g·L^{-1} Glu in Hank's solution inhibit the corrosion of pure Mg as the Glu content increased[39]. In contrast, in this study, the increase in Glu concentration in Hank's solution accelerated the corrosion of Mg-4Li-1Ca alloy, which can be related to the presence of galvanic coupling corrosion between the large amount of anodic second phase and α-Mg in the alloy. Imani et al.[69] found that the addition of 0.1 g·L^{-1} of BSA to 2 g·L^{-1} of Glu in SBF solution inhibited the corrosion of WE43 alloy, which was consistent with the fact that BSA addition inhibited the corrosion of Mg alloy in this experiment.

In comparison to the EFC morphology of Mg-1Li-1Ca in 3.5 wt.% NaCl solution with long-term immersion[14], the EFC of the Mg-4Li-1Ca alloy in Hank's solution was less seriously due to the presence of phosphates and the protective nature of the Hank's solution. The macroscopic peeling of Mg-4Li-1Ca alloy in Hank's solution tends to be single or several layers warped as compared to the book-bound-like multi-layer peeling observed in Mg-1Li-1Ca in 3.5 wt.% NaCl solution[14] and also in Al alloys in the marine atmosphere[23].

The effect of organic molecules on the degradation behavior of Mg alloys has been widely reported[4,70], but the most studies show the results of short-term degradation. However, for bone implant applications, the material must maintain their mechanical properties in the human body for at least 12 weeks. Hence, the effect of organic molecules on the long-term degradation of Mg alloys is critical. Moreover, the effect of organic molecules on the degradation of Mg alloys may change with time. Hereby, the EFC mechanism of Mg-4Li-1Ca alloy during long-term immersion were investigated under the coupling of Glu and BSA.

Mg is a very reactive in salt solutions. Initially, Mg in solution produces large amounts of Mg^{2+}, OH^- and H_2 molecules. As a result, the pH of the solution increases. The chemical reactions involved in the dissolution of Mg are listed below:

$$Mg(s) \rightarrow Mg^{2+}(aq) + 2e^-(\text{Anode reaction}) \quad (1)$$

$$2H_2O + 2e^- \rightarrow H_2(g) + 2OH^-(aq)(\text{Cathodic reaction}) \quad (2)$$

$$Mg^{2+}(aq) + 2OH^-(aq) \rightarrow Mg(OH)_2(s)(\text{Product generation}) \quad (3)$$

Many of the secondary phase particles (i.e., $Mg_{17}Al_{12}$, $A_{l8}Mn_5$, Mg_2Si, etc.) in Mg alloys are found to be cathodic in nature due to α-Mg substrate possessing low electrode potential. However, certain second phases have been identified as anodic (e.g., Mg_2Ca, $(Mg, Al)_2Ca$, $Mg_{60}Zn_{32}Nd_8$, $Mg_{35}Zn_{40}Nd_{25}$[71], $Mg_{41}Nd_5$[16]), resulting in differences in the corrosion mechanisms and dissolution rates of Mg alloys[9,72]. In Mg-Ca alloys, the secondary phase particles Mg_2Ca have been found to be more negative[73] and have a lower i_{corr}[53] than that of the α-Mg substrate. Hence, Mg_2Ca particles undergo selective corrosion in Mg-Ca alloys.

Ding et al.[14] reported that EFC of extruded Mg-1Li-1Ca alloys must include two conditions: (i) structural factors, and (ii) corrosion factors. For Mg-4Li-1Ca, a pattern of lamellar distribution of the Mg_2Ca anodic second phase particles in the alloy can be observed from metallography, EBSD, and SKP. Furthermore, the Mg_2Ca particles being anodic corrodes preferentially in Hank's solution, and thus providing an active channel for Mg-4Li-1Ca EFC.

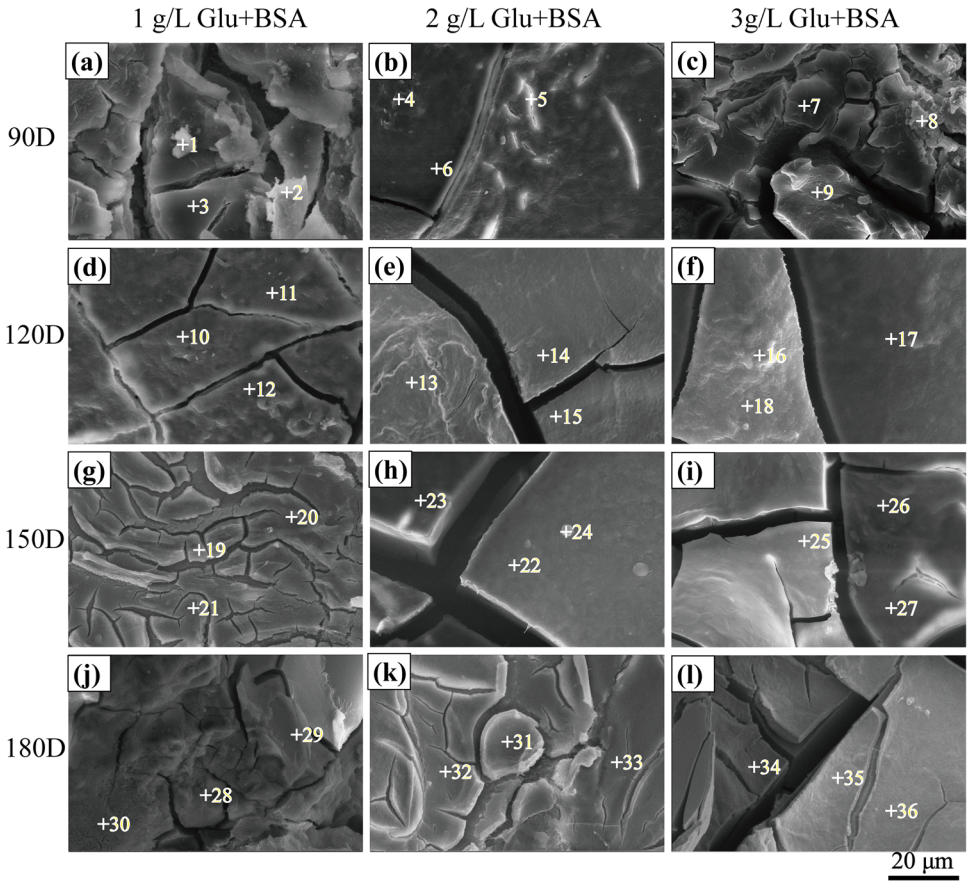

Fig. 8 SEM of the surface of Mg-4Li-1Ca alloy after different immersion times containing BSA at different concentrations of Glu. a 1 g·L^{-1} Glu + BSA 90 D, **b** 1 g·L^{-1} Glu + BSA 120 D, **c** 1 g·L^{-1} Glu + BSA 150 D, **d** 1 g·L^{-1} Glu + BSA 180 D, **e** 2 g·L^{-1} Glu + BSA 90 D, **f** 2 g·L^{-1} Glu + BSA 120 D, **g** 2 g·L^{-1} Glu + BSA 150 D, **h** 2 g·L^{-1} Glu + BSA 180 D, **i** 3 g·L^{-1} Glu + BSA 90 D, **j** 3 g·L^{-1} Glu + BSA 120 D, **k** 3 g·L^{-1} Glu + BSA 150 D, **l** 3 g·L^{-1} Glu + BSA 180 D.

PBR is the ratio of the volume V_{com} of a compound to the volume V_M of a metal, as shown in the following equation[14]:

$$PBR = \frac{V_{com}}{V_M} = \frac{M_{com} \bullet \rho_M}{n \bullet A \bullet \rho_{com}} \quad (4)$$

where M_{com} and ρ_{com} are the molecular weight and density of the compound, respectively. A and ρ_M are the atomic weight and density of the metal, and n is the number of metal atoms in the molecule of the compound.

The second phase particles, Mg_2Ca, had a lower electrode potential than the α-Mg phase[74] and it acted as an active channel for corrosion reactions, and the resulting corrosion products deposited in the active channel. As the PBR of these corrosion products was greater than 1, there was a significant wedging effect. The active channels of the corrosion reaction could gradually penetrate deeper into the substrate, eventually producing corrosion cracks and the corrosion products buckling the lamellar alloy to make it peel off the substrate.

The EBSD results indicated that the Mg-4Li-1Ca alloy grains showed a clear texture along the extrusion direction, which provided a location for the lamellar distribution of the second phase particles. The preferential dissolution of the intermetallic compounds Mg_2Ca resulted in the occurrence of EFC. Moreover, it was also evident from the LAM diagram that residual stresses existed within the alloy, and the high-energy at the residual stresses accelerated corrosion[75,76], while the residual stresses at the LS tended to be distributed along the extrusion direction, accelerating the corrosion cracks along the extrusion direction.

Previous studies had shown that Glu was converted in solution from aldehyde groups to carboxyl groups and thus to gluconic acid, which promoted the enrichment of Cl^- (Eq. 5, 6)[39]. The Cl^- ions attacked the corrosion product $Mg(OH)_2$ ($K_{sp} = 9.628 \times 10^{-4}$) on the alloy surface to produce soluble $MgCl_2$ ($K_{sp} = 54.6$), leading to the breakdown of the surface film and promoting further corrosion of the Mg-4Li-1Ca alloy (Eq. 7). Therefore, the increase in Glu concentration in Hank's solution accelerated EFC (Fig. 15a).

$$CH_2OH(CHOH)_4CHO \xrightarrow{O_2,37^\circ C} RCOOH \quad (5)$$

$$2RCOOH + Mg(OH)_2 \rightarrow (RCOO)_2Mg + 2H2O \quad (6)$$

$$Mg(OH)_2 + Cl^- \rightarrow MgCl_2 + 2OH^- \quad (7)$$

Mg-4Li-1Ca alloy did not show any macroscopic EFC morphology until 120 days in Hank's solution containing BSA, which suggest that BSA inhibited the occurrence of EFC. However, lowering the Glu content in the solution, EFC became more severe. The EFC mechanism in Mg-4Li-1Ca alloy is illustrated in Fig. 15b. It has been previously shown that amino acids reacted with Glu to form a new compound containing -C = N-, a Schiff base, and that amino acids could also form Glu-amino acid amides with amino acids in proteins (Eq. 8)[41,43]. This allows Glu to promote the adsorption of proteins on the Mg alloy surface. Consistent results were derived from the fluorescent labeling experiments (Fig. 15b). Due to the preferential corrosion of Mg_2Ca, the corrosion produced large amounts of Mg^{2+} and Ca^{2+}. Glu and protein

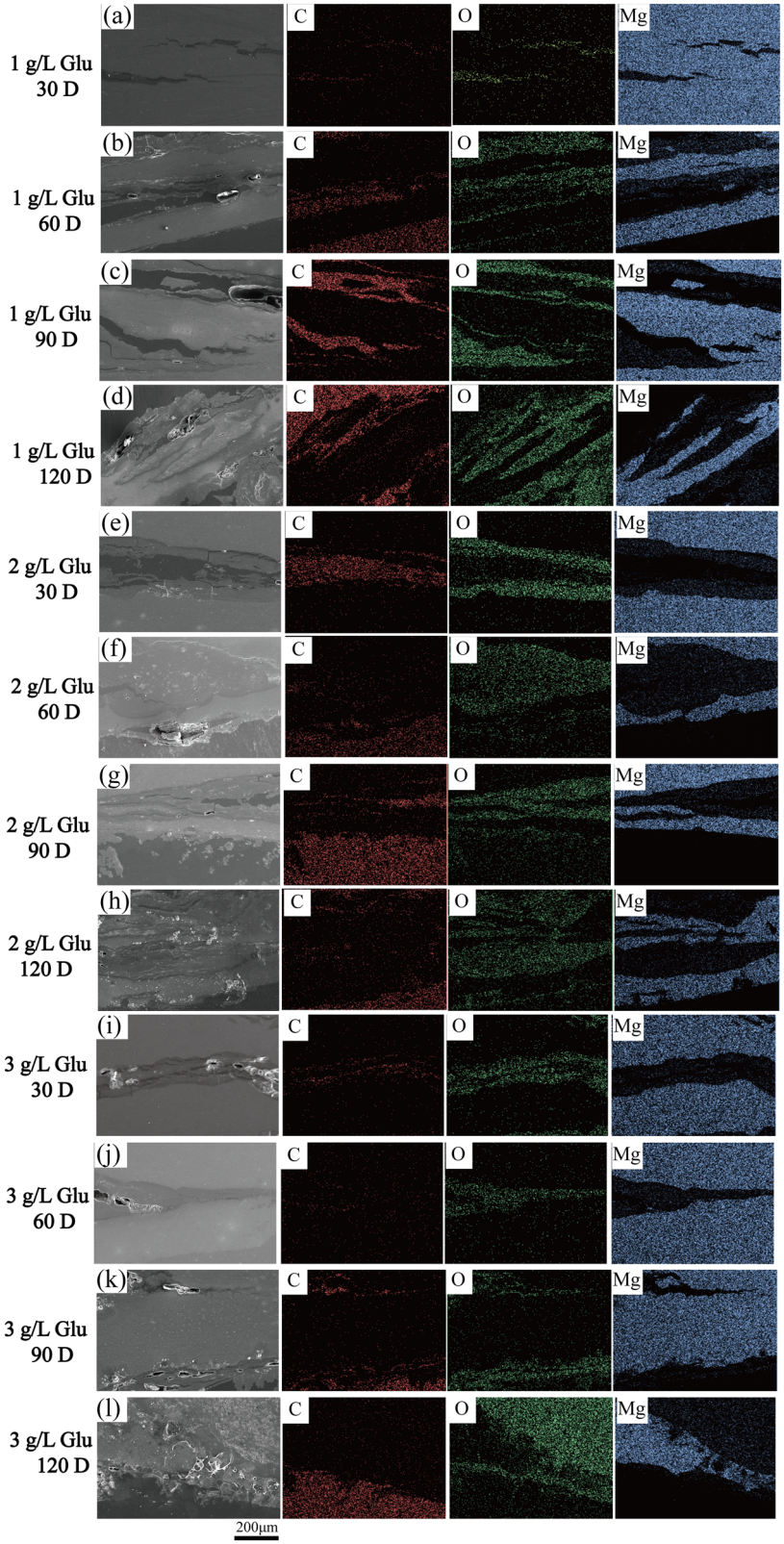

Fig. 9 Cross-SEM and EDS of the surface of Mg-4Li-1Ca alloy after different immersion times at different concentrations of Glu. **a** 1 g·L^{-1} Glu 30 D, **b** 1 g·L^{-1} Glu 60 D, **c** 1 g·L^{-1} Glu 90 D, **d** 1 g·L^{-1} Glu 120 D, **e** 2 g·L^{-1} Glu 30 D, **f** 2 g·L^{-1} Glu 60 D, **g** 2 g·L^{-1} Glu 90 D, **h** 2 g·L^{-1} Glu 120 D, **i** 3 g·L^{-1} Glu 30 D, **j** 3 g·L^{-1} Glu 60 D, **k** 3 g·L^{-1} Glu 90 D, **l** 3 g·L^{-1} Glu 120 D.

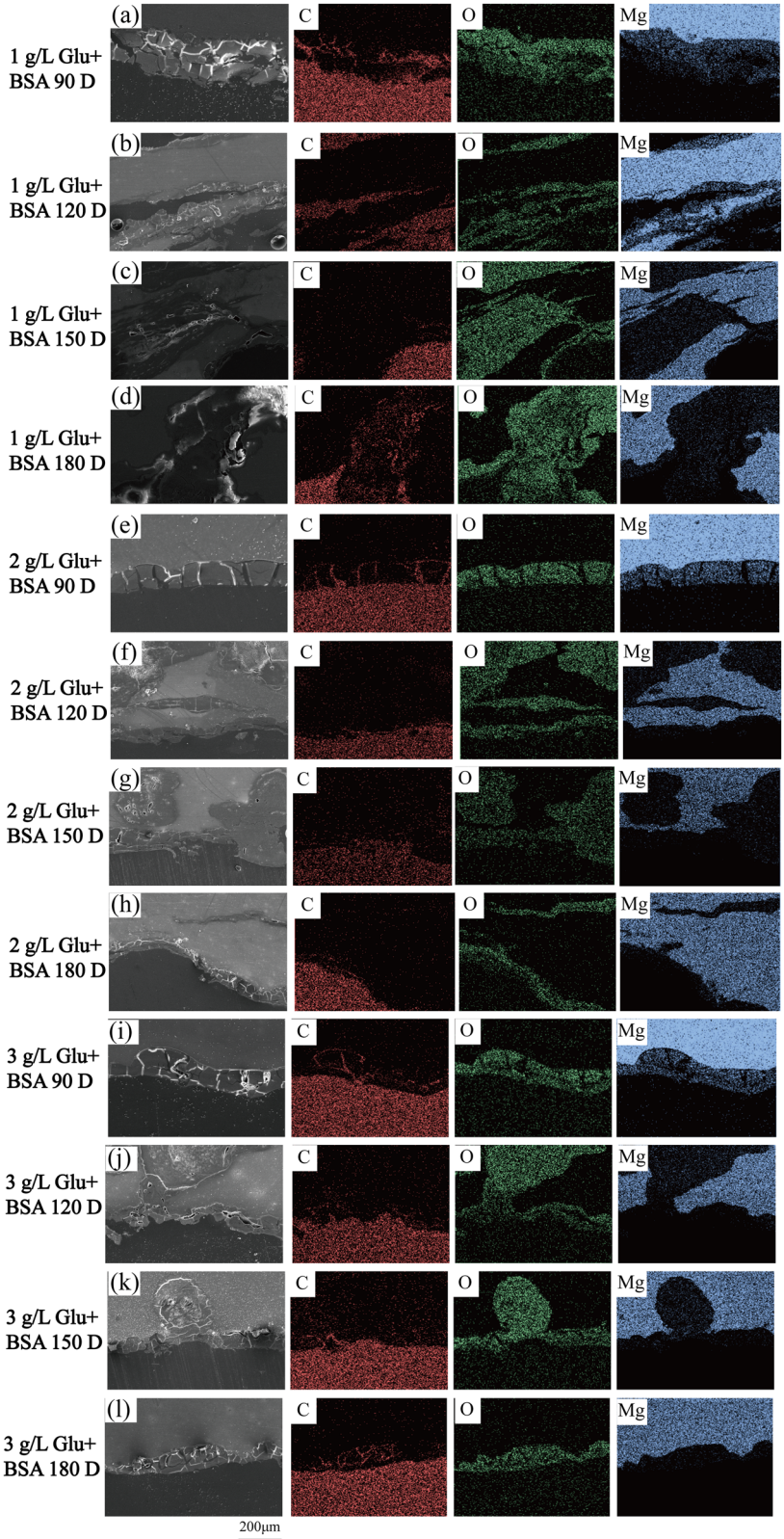

Fig. 10 Cross-SEM and EDS of the surface of Mg-4Li-1Ca alloy after different immersion times containing BSA at different concentrations of Glu. a 1 g·L^{-1} Glu + BSA 90 D, **b** 1 g·L^{-1} Glu + BSA 120 D, **c** 1 g·L^{-1} Glu + BSA 150 D, **d** 1 g·L^{-1} Glu + BSA 180 D, **e** 2 g·L^{-1} Glu + BSA 90 D, **f** 2 g·L^{-1} Glu + BSA 120 D, **g** 2 g·L^{-1} Glu + BSA 150 D, **h** 2 g·L^{-1} Glu + BSA 180 D, **i** 3 g·L^{-1} Glu + BSA 90 D, **j** 3 g·L^{-1} Glu + BSA 120 D, **k** 3 g·L^{-1} Glu + BSA 150 D, **l** 3 g·L^{-1} Glu + BSA 180 D.

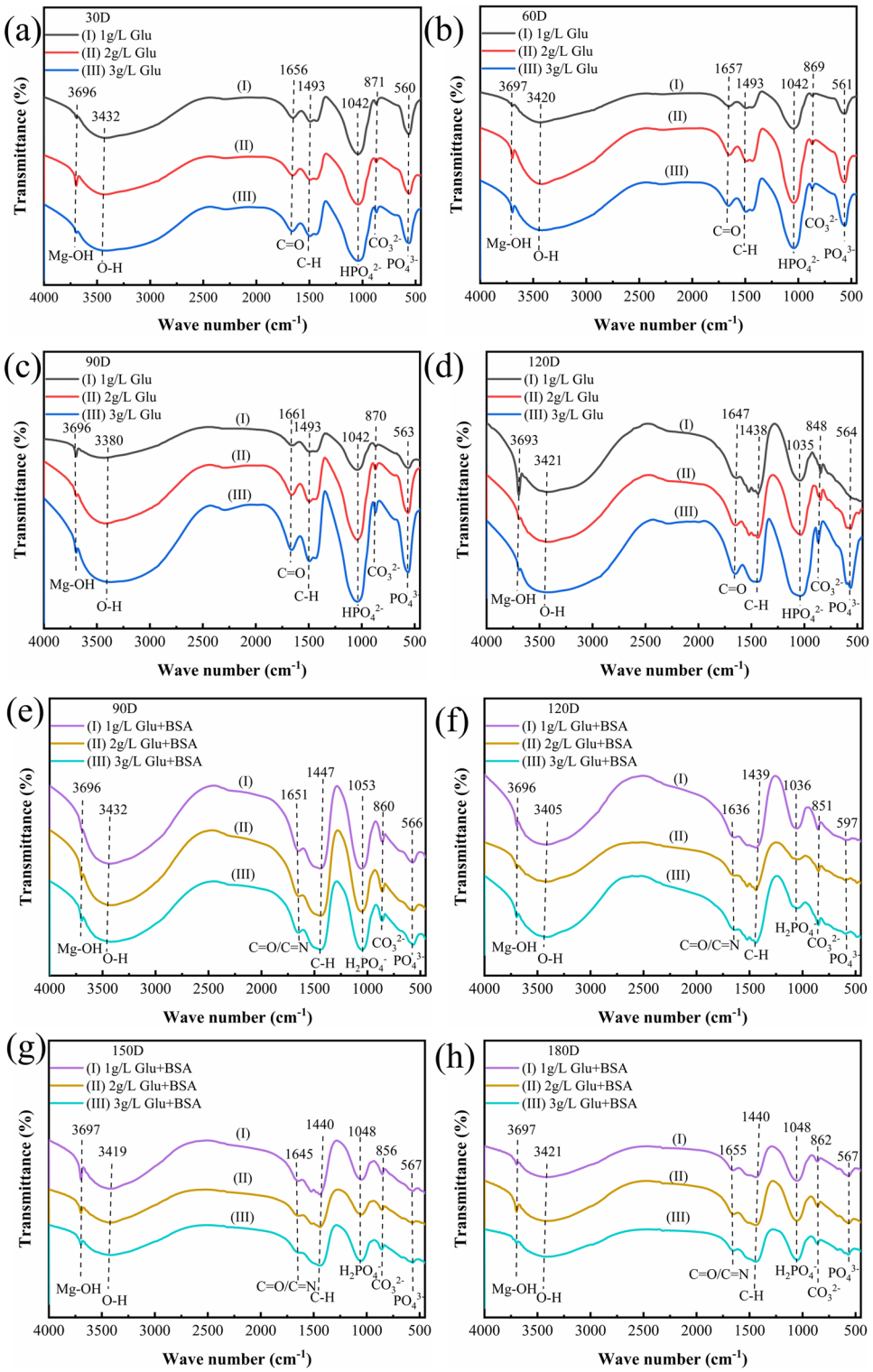

Fig. 11 FT-IR of the surface of the Mg-4Li-1Ca alloy after immersion in different concentrations of Glu for different times. Without BSA **a** 30 days, **b** 60 days, **c** 90 days, **d** 120 days, and with BSA **e** 90 days, **f** 120 days, **g** 150 days, and **h** 180 days.

complexed with Mg^{2+} and Ca^{2+}, Ca^{2+} had stronger complexation with gluconic acid and proteins[45] and the increased surface roughness after corrosion allowed Glu and BSA to preferentially adsorb in the second phase. As the immersion time increased, the proteins produced a dense protective film on the Mg alloy surface, which allowed the Mg alloy to change from localized corrosion (pitting, preferential corrosion of the second phase particles) to uniform corrosion, inhibiting the occurrence of spalling. As the immersion time increases, the sample surface layer was corroded away. Previously, our group has found that EFC of Mg-Li-Ca alloys was more likely to occur after the removal of the surface layer. Hence, after corrosion of the surface layer, the Mg-4Li-1Ca alloy

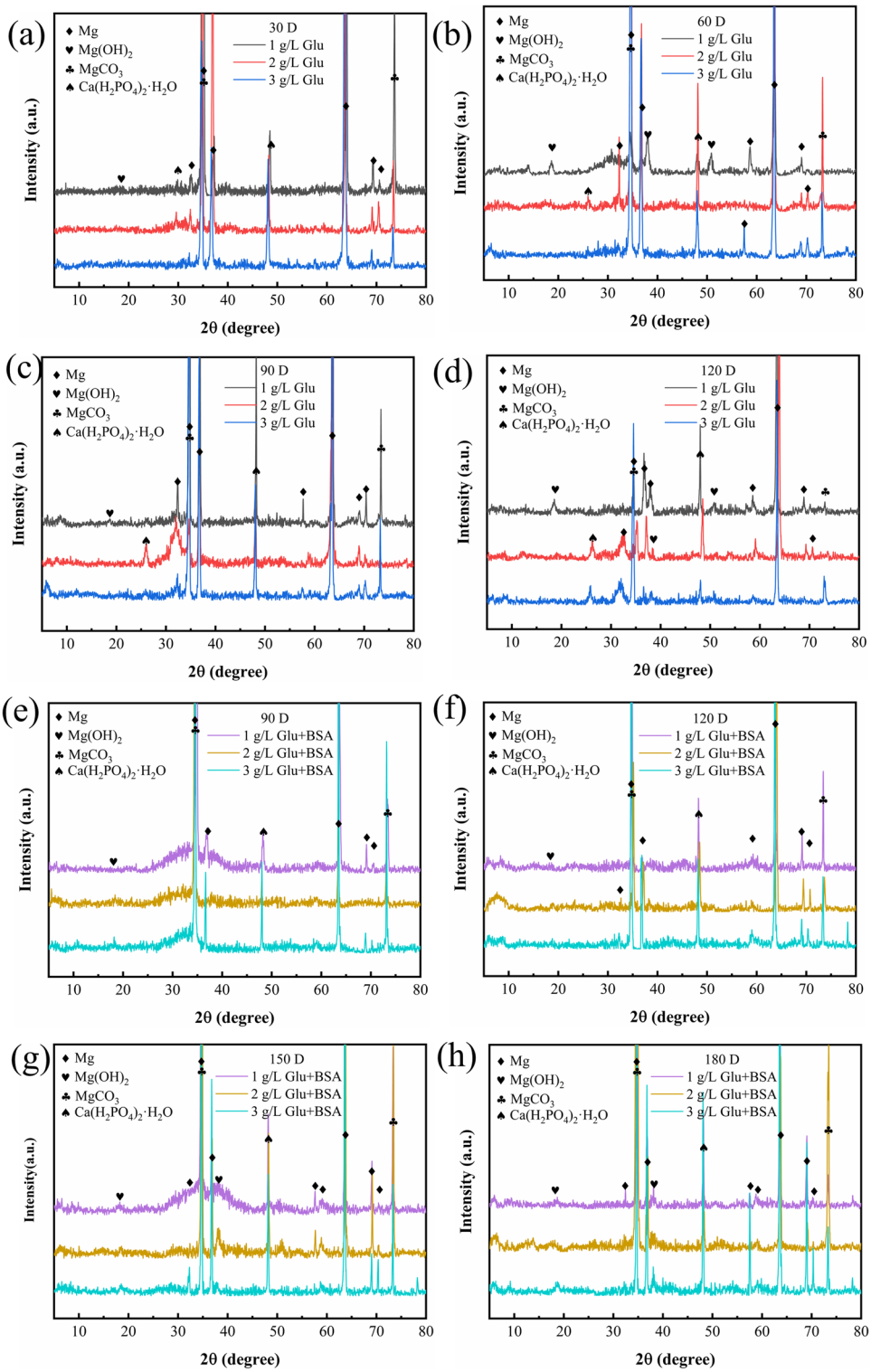

Fig. 12 XRD patterns of the surface of the Mg-4Li-1Ca alloy after immersion in different concentrations of Glu for different times. Without BSA **a** 30 days, **b** 60 days, **c** 90 days, **d** 120 days, and with BSA **e** 90 days, **f** 120 days, **g** 150 days, and **h** 180 days.

EFC occurs due to a combination of structural and corrosion factors, stresses, hydrogen bubbles, etc.

$$R-NH_2 + R'-COH \rightarrow R-N=CH-R' + H_2O \quad (8)$$

In summary this study investigated the effects of different concentrations of Glu and protein in Hank's solution on the EFC behviour of Mg-4Li-1Ca alloy. The main findings are summarized as follows:

(1) Microstructural analysis of the Mg-4Li-1Ca alloy using optical metallography and scanning Kelvin probe measurements reveal that the anodic second phase Mg_2Ca particles were distributed in a lamellar pattern along the grain boundaries

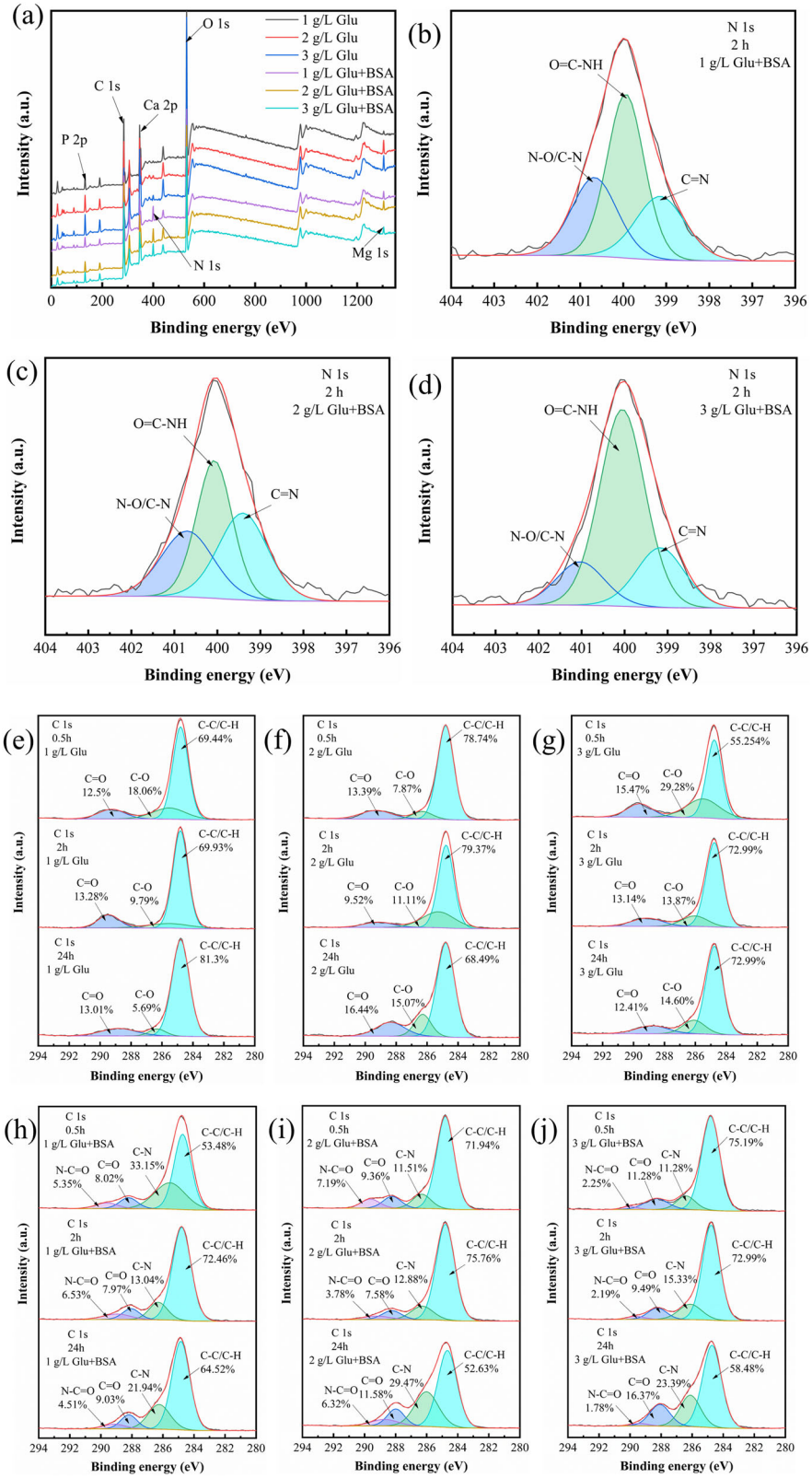

Fig. 13 XPS analysis of the Mg-4Li-1Ca alloy immersed in different solutions. Immersion for 2 h **a** XPS broad survey and N1s spectra **b** 1 g·L^{-1} Glu + BSA, **c** 2 g·L^{-1} Glu + BSA, **d** 3 g·L^{-1} Glu + BSA; C1s spectra after different times (0.5 h, 2 h, 24 h) **e** 1 g·L^{-1} Glu, **f** 2 g·L^{-1} Glu, **g** 3 g·L^{-1} Glu, **h** 1 g·L^{-1} Glu + BSA, **i** 2 g·L^{-1} Glu + BSA, and **j** 3 g·L^{-1} Glu + BSA.

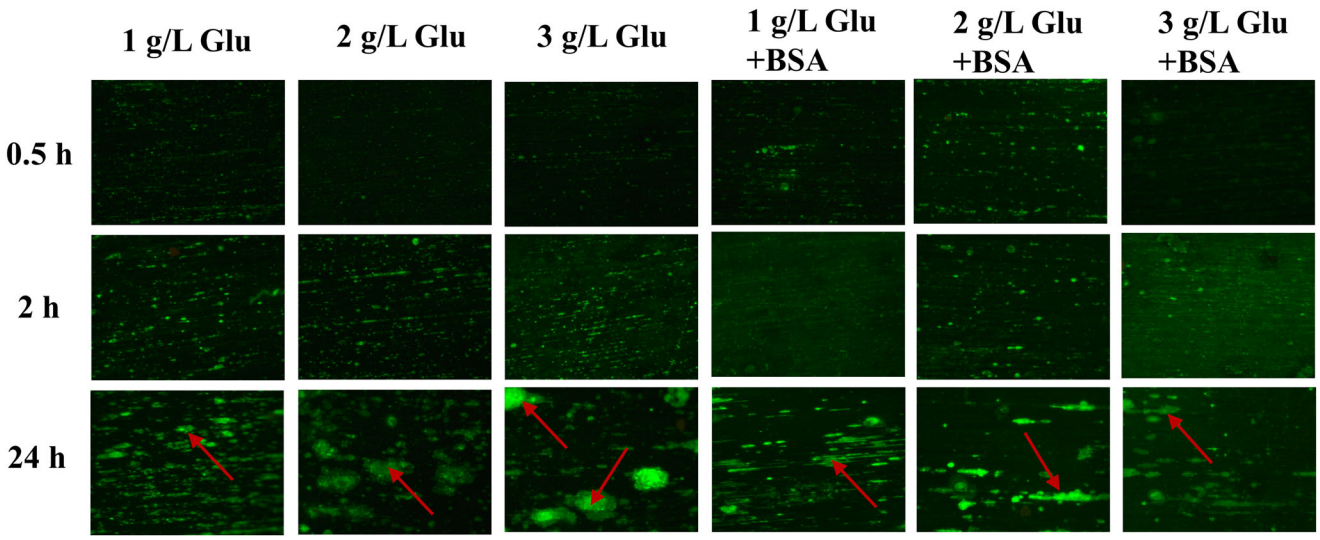

Fig. 14 Fluorescent labeling spectra. Fluorescent labeling spectra of the surface of the Mg-4Li-1Ca alloy after immersion in different concentrations of Glu and in the presence of BSA for different times.

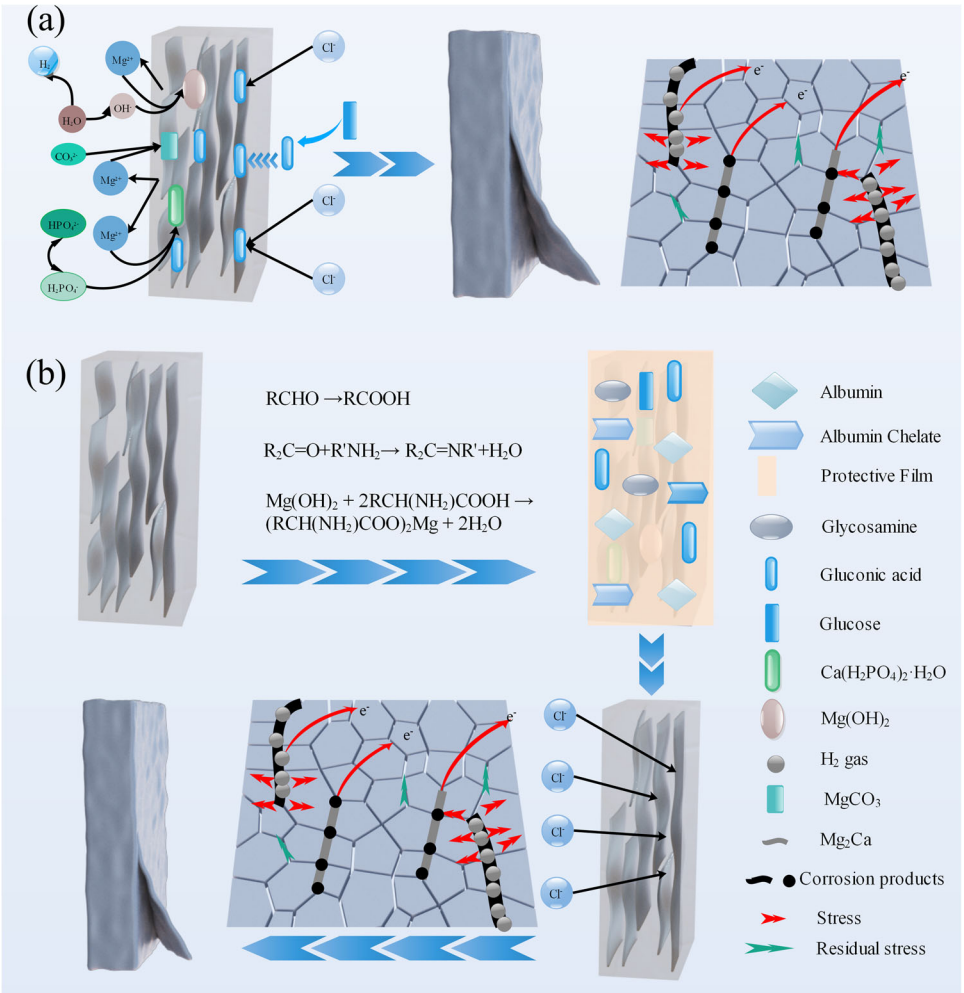

Fig. 15 EFC mechanism of Mg-4Li-1Ca alloy in Hank's solution. a Without BSA, **b** with BSA.

in the extrusion direction. Mg_2Ca had a lower Volta potential and the surface layer of the alloy had a higher Volta potential for greater corrosion resistance. And from the EBSD, the alloy had significant weaving and residual stresses. This lamellar distribution facilitated the preferential corrosion of Mg_2Ca along the grain boundaries, thus creating the conditions for EFC. Moreover, the texture and the presence of residual stresses of the alloy accelerated the occurrence of EFC.

(2) Mg-4Li-1Ca alloy exhibited EFC after 30 days of immersion in Hank's solution. Higher Glu content resulted in more severe EFC. However, when BSA was present in Hank's solution, macroscopic EFC morphology was observed only after 120 days of immersion, indicating that BSA inhibited EFC. But lower Glu content resulted in more severe EFC in this condition.

(3) Fluorescent labeling showed that Glu and protein were mainly present on the second phase particles, which were preferentially corroding due to their anodic nature. The Mg^{2+} and Ca^{2+} generated during corrosion, interact with the carboxyl groups in gluconic acid and the carboxyl and amino groups in proteins, leading to chelation and electrostatic adsorption. Glu and protein coupled and adsorbed, formed a dense protective film on Mg-4Li-1Ca surface, which transformed the corrosion from localized corrosion (pitting, preferential corrosion at the second phase) to uniform corrosion, and inhibiting further corrosion.

(4) Analysis by EDS, FT-IR, XRD, and XPS showed that the corrosion products were mainly $MgCO_3$, $Ca(H_2PO_4)_2{\cdot}H_2O$, and $Mg(OH)_2$, along with chelation complexes of Glu (or albumin) and metal cations.

Overall, this study provides valuable insights into the microstructural characteristics and corrosion behavior of the Mg-4Li-1Ca alloy, and enriching the literature on the corrosion types in biomedical Mg-based alloys, and potentially facilitates the improvement in the EFC resistance of the alloys.

METHODS

Materials preparation

In this study, Mg-4Li-1Ca alloy (chemical composition: Li 3.71 wt.%, Ca 1.15 wt.%, and Mg balance) was used as the test material. The alloy was extruded with a 30:1 extrusion ratio at a rate of 1 m•min^{-1}, with the mold and extrusion temperatures set at 350 and 300 °C, respectively. The extruded sheets were then cut into rectangular specimens (20 mm × 10 mm × 4.5 mm) in different sections, as illustrated in Supplementary Fig. 1. Small holes were drilled at one end of the specimens to facilitate suspension using a string for the immersion test. Prior to the immersion, the specimens were ground with wet SiC abrasive paper (grit sizes ranging from 150 to 1500), and then polished with 1.0 μm diamond paste to obtain a mirror surface.

Microstructure observation

The microstructure and chemical composition of Mg-4Li-1Ca alloy were examined using optical microscopy (OM, ZEISS Axio Lab A1, Germany) and EPMA (JXA-8230, Japan). Prior to OM observation, specimens were chemically etched with a solution consisting 100 ml deionized water, 1.5 ml nitric acid (65–68%), 1 g oxalic acid, and 1 ml acetic acid (99%) at room temperature for 30 s.

Electrochemical behavior

Electrochemical measurements were conducted using a three-electrode cell setup and an electrochemical workstation (Princeton VersaSTAT 4). The cell setup consisted of a standard three-electrode configuration, with a platinum foil electrode serving as the counter electrode, a saturated calomel electrode (SCE) as the reference electrode, and Mg-4Li-1Ca alloy as the working electrode. The tests were conducted in physiological environment at room temperature. The OCP was measured for the first 3600 s of immersion. EIS test was carried out in a frequency range from 100 kHz to 0.1 Hz, and the PDP were carried out from −0.4 V to 0.6 V (vs. OCP) with a scan rate of 1 mV•s^{-1}. The repeatability of each test was ensured in triplicate. Moreover, E_{corr} and i_{corr} are estimated by Tafel extrapolation from the anodic and cathodic polarization zones where the overpotential is 60 mV lower or higher than the free corrosion potential.

Scanning Kelvin probe measurement

Volta potential maps were generated using a SKP (Princeton VERSA SCAN). The measurements were conducted under an air relative humidity of 65%. The probe, made of tungsten with a diameter of 500 μm, was positioned at a fixed height above the sample surface. A square scanning area of 1000 μm × 1000 μm was used with a scanning step of 50 μm in both the X and Y directions.

Immersion tests

The surface finished samples were suspended in 500 mL beakers using cotton strings. The beakers (with three samples in each beaker) were placed in an electrothermal thermostat (DHP-420AB, Tianjin Sedeli Experimental Analytical Instruments Manufacturing, China) at 37 ± 0.5 °C. The solution was changed every three days to prevent the solution from deteriorating and growing bacteria. The samples were removed after 30, 60, 90, and 120 days of immersion for the samples in Hank's solutions with different concentrations of Glu (1, 2, 3 g•L^{-1}, since plasma glucose levels range from 4.6 to 6.1 mmol•L^{-1} in normal subjects, 10 mmol•L^{-1} after a meal, and 15 mmol•L^{-1} in hyperglycemic subjects[77]). The samples were immersed in Hank's solution containing BSA (0.1 g•L^{-1}, i.e., the concentration of BSA in human plasma[43]) with different concentrations of Glu for 90, 120, 150, and 180 days. Three samples were immersed in each condition to ensure the accuracy of the experiment. The removed samples were rinsed with deionised water, dried using a hairdryer and stored in a sealed container for subsequent analysis and testing. In this experiment, Hank's solution was chosen as the corrosion medium to study the influence of different levels of Glu and BSA on the susceptibility of EFC in Mg-4Li-1Ca. The chemical composition of the solution used for the immersion test is listed in Supplementary Table 1.

Surface characterization

The morphology and cross-section of the samples after immersion for different durations were captured using a digital camera. The chemical composition of the samples was identified using field emission scanning electron microscopy (FE-SEM, Nova Nano SEM450, USA) and EDS (Oxford X-MaxN). Corrosion products were examined using XRD (Rigaku D/MAX 2500PC, Japan), FT-IR (Nicolet 380; Thermo electron, US), and XPS (ESCALAB250Xi). Fluorescence microscopy (FM, Leica DM2500, Germany) was employed to detect the presence of Glu and albumin.

DATA AVAILABILITY

The data that support the findings of this study are available from Prof. Rong-Chang Zeng (Email: rczeng@foxmail.com) upon reasonable request.

CODE AVAILABILITY

The codes that support the findings of this study are available from the corresponding author upon reasonable request.

Received: 27 September 2023; Accepted: 2 January 2024;
Published online: 17 January 2024

REFERENCES

1. Yang, Y. et al. Research advances in magnesium and magnesium alloys worldwide in 2020. *J. Magnes. Alloy.* **9**, 705–747 (2021).
2. Li, L. Y. et al. Advances in functionalized polymer coatings on biodegradable magnesium alloys—a review. *Acta Biomater.* **79**, 23–36 (2018).
3. Pan, S.-Q., Zhang, F., Wen, C. & Zeng, R.-C. Advances in Mg–Al-layered double hydroxide steam coatings on Mg alloys: a review. *J. Magnes. Alloy.* **11**, 1505–1518 (2023).
4. Cai, L. et al. Advances in bioorganic molecules inspired degradation and surface modifications on Mg and its alloys. *J. Magnes. Alloy.* **10**, 670–688 (2022).
5. Li, D. et al. In vitro and in vivo assessment of the effect of biodegradable magnesium alloys on osteogenesis. *Acta Biomater.* **141**, 454–465 (2022).
6. Costantino, M. D. et al. Inflammatory response to magnesium-based biodegradable implant materials. *Acta Biomater.* **101**, 598–608 (2020).
7. Zhao, Y. et al. pH/NIR-responsive and self-healing coatings with bacteria killing, osteogenesis, and angiogenesis performances on magnesium alloy. *Biomaterials* **301**, 122237 (2023).
8. Jiao, Z.-J. et al. In vitro degradation and biocompatibility of in-situ fabricated Mg-Al-Ga-LDH/MAO hybrid coating on Mg alloy AZ31. *Surf. Coat. Technol.* **472**, 129922 (2023).
9. Zeng, R. C., Cui, L. Y. & Ke, W. Biomedical magnesium alloys: composition, microstructure and corrosion. *Acta Metall. Sin.* **54**, 1215–1235 (2018).
10. Jia, J. X., Atrens, A., Song, G. & Muster, T. H. Simulation of galvanic corrosion of magnesium coupled to a steel fastener in NaCl solution. *Mater. Corros.* **56**, 468–474 (2005).
11. Lafront, A. M. et al. Pitting corrosion of AZ91D and AJ62x magnesium alloys in alkaline chloride medium using electrochemical techniques. *Electrochim. Acta* **51**, 489–501 (2005).
12. Andreatta, F., Apachitei, I., Kodentsov, A. A., Dzwonczyk, J. & Duszczyk, J. Volta potential of second phase particles in extruded AZ80 magnesium alloy. *Electrochim. Acta* **51**, 3551–3557 (2006).
13. Zeng, R., Kainer, K. U., Blawert, C. & Dietzel, W. Corrosion of an extruded magnesium alloy ZK60 component—the role of microstructural features. *J. Alloy. Compd.* **509**, 4462–4469 (2011).
14. Ding, Z.-Y. et al. Exfoliation corrosion of extruded Mg-Li-Ca alloy. *J. Mater. Sci. Technol.* **34**, 1550–1557 (2018).
15. Morishige, T. H., Goto, T., Nakamura, E. & Takenaka, T. J. M. T. Exfoliation corrosion behavior of cold-rolled Mg-14 mass% Li-1 mass% Al alloy in NaCl solution. *Mater. Trans.* **54**, 1863–1866 (2013).
16. Gao, G.-J. et al. Dealloying corrosion of anodic and nanometric Mg41Nd5 in solid solution-treated Mg-3Nd-1Li-0.2Zn alloy. *J. Mater. Sci. Technol.* **83**, 161–178 (2021).
17. Unigovski, Y., Eliezer, A., Abramov, E., Snir, Y. & Gutman, E. M. Corrosion fatigue of extruded magnesium alloys. *Mater. Sci. Eng. A* **360**, 132–139 (2003).
18. Zeng, R., Qi, W., Zhang, F., Cui, H. & Zheng, Y. In vitro corrosion of Mg–1.21Li–1.12Ca–1Y alloy. *Prog. Nat. Sci. Mater. Int.* **24**, 492–499 (2014).
19. Song, Y., Shan, D., Chen, R. & Han, E.-H. Corrosion characterization of Mg–8Li alloy in NaCl solution. *Corros. Sci.* **51**, 1087–1094 (2009).
20. Ding, Z.-Y. et al. In vitro corrosion of micro-arc oxidation coating on Mg-1Li-1Ca alloy—the influence of intermetallic compound Mg2Ca. *J. Alloy. Compd.* **764**, 250–260 (2018).
21. Chen, B. et al. In vitro crevice corrosion of biodegradable magnesium in different solutions. *J. Mater. Sci. Technol.* **52**, 83–88 (2020).
22. Esmaily, M. et al. Fundamentals and advances in magnesium alloy corrosion. *Prog. Mater. Sci.* **89**, 92–193 (2017).
23. Sun, S., Fang, Y., Zhang, L., Li, C. & Hu, S. Effects of aging treatment and peripheral coarse grain on the exfoliation corrosion behaviour of 2024 aluminium alloy using SR-CT. *J. Mater. Res. Technol.* **9**, 3219–3229 (2020).
24. Song, G. L. & Atrens, A. Corrosion mechanisms of magnesium alloys. *Adv. Eng. Mater.* **1**, 11–33 (1999).
25. Song, J., She, J., Chen, D. & Pan, F. Latest research advances on magnesium and magnesium alloys worldwide. *J. Magnes. Alloy.* **8**, 1–41 (2020).
26. Ghorbani, M., Boley, M., Nakashima, P. N. H. & Birbilis, N. A machine learning approach for accelerated design of magnesium alloys. *J. Magnes. Alloy.* **11**, 3620–3633 (2023).
27. Witte, F. et al. In vitro and in vivo corrosion measurements of magnesium alloys. *Biomaterials* **27**, 1013–1018 (2006).
28. Yurchenko, N. Y. et al. Effect of multiaxial deformation on structure, mechanical properties, and corrosion resistance of a Mg-Ca alloy. *J. Magnes. Alloy.* **10**, 266–280 (2022).
29. Zeng, R. et al. Study on corrosion of medical Mg–Ca and Mg–Li–Ca alloys. *Acta Metall. Sin.* **47**, 1477–1482 (2011).
30. Zeng, R.-C., Sun, L., Zheng, Y.-F., Cui, H.-Z. & Han, E.-H. Corrosion and characterisation of dual phase Mg–Li–Ca alloy in Hank's solution: the influence of microstructural features. *Corros. Sci.* **79**, 69–82 (2014).
31. Long, L.-X. et al. Comparison of microstructure, mechanical property, and degradation rate of Mg–1Li–1Ca and Mg–4Li–1Ca alloys. *Bioact. Mater.* **26**, 279–291 (2023).
32. Cui, L., Sun, L., Zeng, R., Zheng, Y. & Li, S. In vitro degradation and biocompatibility of Mg-Li-Ca alloys—the influence of Li content. *Sci. China Mater.* **61**, 607–618 (2017).
33. Xia, D. et al. In vitro and in vivo investigation on biodegradable Mg-Li-Ca alloys for bone implant application. *Sci. China Mater.* **62**, 256–272 (2018).
34. Wang, Y. et al. Corrosion behavior and mechanical property of Mg-4Li-1Ca alloys under micro-compressive stress. *J. Mater. Sci. Technol.* **175**, 170–184 (2024).
35. *IDF Diabetes Atlas*, https://diabetesatlas.org/atlas/tenth-edition/ (2021).
36. Nanditha, A. et al. Diabetes in Asia and the Pacific: Implications for the Global Epidemic. *Diabetes Care* **39**, 472–485 (2016).
37. Verma, A. K. et al. A compendium of perspectives on diabetes: a challenge for sustainable health in the modern era. *Diabetes Metab. Syndr. Obes.* **14**, 2775–2787 (2021).
38. Anastasilakis, A. D. et al. The impact of antiosteoporotic drugs on glucose metabolism and fracture risk in diabetes: good or bad news? *J. Clin. Med* **10**, 996 (2021).
39. Zeng, R. C., Li, X. T., Li, S. Q., Zhang, F. & Han, E. H. In vitro degradation of pure Mg in response to glucose. *Sci. Rep.* **5**, 13026 (2015).
40. Cui, L.-Y. et al. In vitro corrosion of Mg–Ca alloy—the influence of glucose content. *Front. Mater. Sci.* **11**, 284–295 (2017).
41. Wang, Y. et al. In vitro degradation of pure magnesium—the effects of glucose and/or amino acid. *Materials* **10**, 725 (2017).
42. Wang, Y. et al. In vitro corrosion of pure Mg in phosphate buffer solution-Influences of isoelectric point and molecular structure of amino acids. *Mater. Sci. Eng. C. Mater. Biol. Appl* **105**, 110042 (2019).
43. Yan, W. et al. In vitro degradation of pure magnesium-the synergetic influences of glucose and albumin. *Bioact. Mater.* **5**, 318–333 (2020).
44. Li, L. Y. et al. Microbial ingress and in vitro degradation enhanced by glucose on bioabsorbable Mg-Li-Ca alloy. *Bioact. Mater.* **5**, 902–916 (2020).
45. Li, L.-Y. et al. Corrosion resistance of glucose-induced hydrothermal calcium phosphate coating on pure magnesium. *Appl. Surf. Sci.* **465**, 1066–1077 (2019).
46. Mei, D., Wang, C., Lamaka, S. V. & Zheludkevich, M. L. Clarifying the influence of albumin on the initial stages of magnesium corrosion in Hank's balanced salt solution. *J. Magnes. Alloy.* **9**, 805–817 (2021).
47. Wang, H. et al. Influence of the second phase on protein adsorption on biodegradable Mg alloys' surfaces: comparative experimental and molecular dynamics simulation studies. *Acta Biomater.* **129**, 323–332 (2021).
48. Zhang, Z.-Q. et al. Protein conformation and electric attraction adsorption mechanisms on anodized magnesium alloy by molecular dynamics simulations. *J. Magnes. Alloy.* **10**, 3143–3155 (2022).
49. Hou, R.-Q., Scharnagl, N., Willumeit-Roemer, R. & Feyerabend, F. Different effects of single protein vs. protein mixtures on magnesium degradation under cell culture conditions. *Acta Biomater.* **98**, 256–268 (2019).
50. Zhang, Z. Q. et al. Biodegradation behavior of micro-arc oxidation coating on magnesium alloy-from a protein perspective. *Bioact. Mater.* **5**, 398–409 (2020).
51. Sivaraman, B. & Latour, R. A. The adherence of platelets to adsorbed albumin by receptor-mediated recognition of binding sites exposed by adsorption-induced unfolding. *Biomaterials* **31**, 1036–1044 (2010).
52. Hu, X. N. & Yang, B. C. Conformation change of bovine serum albumin induced by bioactive titanium metals and its effects on cell behaviors. *J. Biomed. Mater. Res Part A* **102**, 1053–1062 (2014).
53. Kirkland, N. T. et al. In-vitro dissolution of magnesium-calcium binary alloys: clarifying the unique role of calcium additions in bioresorbable magnesium implant alloys. *J. Biomed. Mater. Res B Appl Biomater.* **95**, 91–100 (2010).
54. Song, G.-L., Mishra, R. & Xu, Z. Crystallographic orientation and electrochemical activity of AZ31 Mg alloy. *Electrochem. Commun.* **12**, 1009–1012 (2010).
55. Song, G.-L. & Xu, Z. Effect of microstructure evolution on corrosion of different crystal surfaces of AZ31 Mg alloy in a chloride containing solution. *Corros. Sci.* **54**, 97–105 (2012).
56. Song, G.-L. & Xu, Z. Crystal orientation and electrochemical corrosion of polycrystalline Mg. *Corros. Sci.* **63**, 100–112 (2012).
57. Calcagnotto, M. E., Ponge, D., Demir, E. & Raabe, D. Orientation gradients and geometrically necessary dislocations in ultrafine grained dual-phase steels studied by 2D and 3D EBSD. *Mater. Sci. Eng. A* **527**, 2738–2746 (2010).
58. Kubin, L. P. & Mortensen, A. Geometrically necessary dislocations and strain-gradient plasticity: a few critical issues. *Scr. Mater.* **48**, 119–125 (2003).

59. Yan, Z. et al. Deformation behaviors and cyclic strength assessment of AZ31B magnesium alloy based on steady ratcheting effect. *Mater. Sci. Eng. A* **723**, 212–220 (2018).
60. Gao, H., Huang, Y., Nix, W. D. & Hutchinson, J. W. Mechanism-based strain gradient plasticity-I. Theory. *J. Mech. Phys. Solids* **47**, 1239–1263 (1999).
61. Song, G., Atrens, A., John, D. S., Wu, X. & Nairn, J. The anodic dissolution of magnesium in chloride and sulfate solutions. *Corros. Sci.* **39**, 1981–2004 (1997).
62. Zhang, C. et al. Ratio of total acidity to pH value of coating bath: a new strategy towards phosphate conversion coatings with optimized corrosion resistance for magnesium alloys. *Corros. Sci.* **150**, 279–295 (2019).
63. Li, C. Q. et al. Composition and microstructure dependent corrosion behaviour of Mg-Li alloys. *Electrochim. Acta* **260**, 55–64 (2018).
64. Zeng, R.-C. et al. Corrosion resistance of Zn–Al layered double hydroxide/poly(-lactic acid) composite coating on magnesium alloy AZ31. *Front. Mater. Sci.* **9**, 355–365 (2015).
65. Mohamad Rodzi, S. N. H., Zuhailawati, H. & Dhindaw, B. K. Mechanical and degradation behaviour of biodegradable magnesium–zinc/hydroxyapatite composite with different powder mixing techniques. *J. Magnes. Alloy.* **7**, 566–576 (2019).
66. Xie, T. et al. Selective C-Terminal Conjugation of Protease-Derived Native Peptides for Proteomic Measurements. *Langmuir* **38**, 9119–9128 (2022).
67. Chen, L. et al. Mg-Zn-Y-Nd coated with citric acid and dopamine by layer-by-layer self-assembly to improve surface biocompatibility. *Sci. China Technol. Sci.* **61**, 1228–1237 (2018).
68. Hou, R. et al. Adsorption of proteins on degradable magnesium-which factors are relevant? *ACS Appl. Mater. Interfaces* **10**, 42175–42185 (2018).
69. Imani, A., Clifford, A. M., Raman, R. K. S. & Asselin, E. Insight into synergetic effects of serum albumin and glucose on the biodegradation behavior of WE43 alloy in simulated body fluid. *Biomed. Mater.* **18**, 015011 (2023).
70. Cai, L. et al. Biodegradation mechanisms of pure Mg in presence of glucose, vitamin C, and citric acid. *Smart Mater. Manuf.* **1**, 100014 (2023).
71. Cai, C., Song, R., Wang, L. & Li, J. Effect of anodic T phase on surface micro-galvanic corrosion of biodegradable Mg-Zn-Zr-Nd alloys. *Appl. Surf. Sci.* **462**, 243–254 (2018).
72. Liu, J. et al. The special role of anodic second phases in the micro-galvanic corrosion of EW75 Mg alloy. *Electrochim. Acta* **189**, 190–195 (2016).
73. Seong, J. W. & Kim, W. J. Mg-Ca binary alloy sheets with Ca contents of ≤1 wt.% with high corrosion resistance and high toughness. *Corros. Sci.* **98**, 372–381 (2015).
74. Südholz, A. D., Kirkland, N. T., Buchheit, R. G. & Birbilis, N. Electrochemical properties of intermetallic phases and common impurity elements in magnesium alloys. *Electrochem. Solid-State Lett.* **14**, C5 (2011).
75. Denkena, B. & Lucas, A. Biocompatible magnesium alloys as absorbable implant materials—adjusted surface and subsurface properties by machining processes. *CIRP Ann.* **56**, 113–116 (2007).
76. Xu, J. et al. New insight into the role of microscale residual stresses on initial corrosion behavior of Ti35 alloy. *Corros. Sci.* **206**, 110491 (2022).
77. Balint, E., Szabo, P., Marshall, C. F. & Sprague, S. M. Glucose-induced inhibition of in vitro bone mineralization. *Bone* **28**, 21–28 (2001).

ACKNOWLEDGEMENTS

This work was supported by the National Natural Science Foundation of China (Grant No. 52071191).

AUTHOR CONTRIBUTIONS

M.B.K., L.Y.C., C.B.L., and R.C.Z. conceptualized this work. L.C. conducted the calculation. L.C., M.Q.Z., M.J.L., J.Y.B., and Y.Q.R. performed the experiments. L.C., L.Y.C., C.B.L., F.Z., and S.Q.L. investigated the results. M.B.K. and R.C.Z. visualized the results. R.C.Z. supervised this work. All authors discussed the results and contributed to the writing of the paper.

COMPETING INTERESTS

The authors declare no competing interests.

ADDITIONAL INFORMATION

Supplementary information The online version contains supplementary material available at https://doi.org/10.1038/s41529-024-00425-1.

Correspondence and requests for materials should be addressed to Rong-Chang Zeng.

Reprints and permission information is available at http://www.nature.com/reprints

Publisher's note Springer Nature remains neutral with regard to jurisdictional claims in published maps and institutional affiliations.